

# Surface Conditions That Constrain Alkane Oxidation on Perovskites

Gregor Koch, Michael Hävecker, Detre Teschner, Spencer J. Carey, Yuanqing Wang, Pierre Kube, Walid Hetaba, Thomas Lunkenbein, Gudrun Auffermann, Olaf Timpe, Frank Rosowski, Robert Schlögl, and Annette Trunschke\*



Cite This: *ACS Catal.* 2020, 10, 7007–7020



Read Online

ACCESS |



Metrics & More



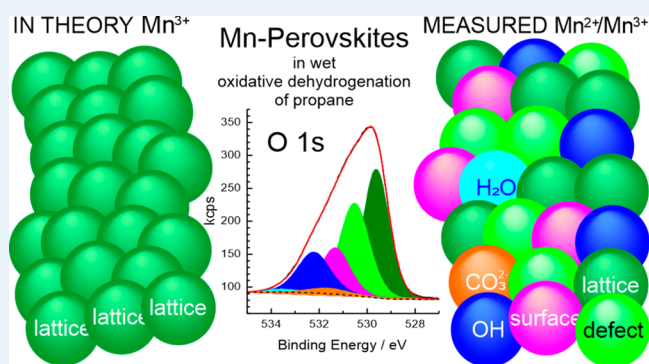
Article Recommendations



Supporting Information

**ABSTRACT:** The crystal structure of perovskites can incorporate a wide variety of cations, which makes this class of materials so interesting for studies of links between solid-state chemistry and catalysis. Perovskites are known as typical total combustion catalysts in hydrocarbon oxidation reactions. The fundamental question that we investigate here is whether surface modifications of perovskites can lead to the formation of valuable reaction products in alkane oxidation. We studied the effect of segregated two-dimensional surface nanostructures on selectivity to propene in the oxidative dehydrogenation of propane. Manganese-based perovskites  $\text{AMnO}_3$  ( $A = \text{La}, \text{Sm}$ ) were prepared by combustion and hydrothermal synthesis. Bulk and surface structures were investigated by X-ray diffraction, temperature-programmed reduction, aberration-corrected scanning transmission electron microscopy (STEM), multiwavelength Raman, and ambient-pressure X-ray photoelectron spectroscopy (AP-XPS) in combination with near-edge X-ray absorption fine structure (NEXAFS) spectroscopy. Surface oxygen species responsible for C–H activation were distinguished by AP-XPS on the basis of a rigorous *in situ* analysis of the O 1s spectra recorded under a broad range of reaction conditions. Signals at 529.2, 530.1, 530.9, 531.2, and 531.8 eV were attributed to lattice O, defect-affected O, surface O, oxygen in carbonates, and hydroxyl groups, respectively. Operando AP-XPS revealed critical surface features, which occur under catalyst operation. The catalyst performance depends on the synthesis technique and the reaction conditions. In presence of a two-dimensional  $\text{MnO}_x$  surface phase, addition of steam to the feed resulted in an increase in selectivity to the partial oxidation product propene to practically relevant values. The selectivity increase is related to the presence of Mn in a low oxidation state ( $2+/3+$ ), an increased concentration of hydroxyl groups, and a higher abundance of adsorbed activated oxygen species on the catalyst surface. The surface analysis of a working catalyst highlights the importance of the termination layer of polycrystalline perovskites as a genuine property implemented by catalyst preparation. Such a termination layer controls the chemical properties and reactivity of perovskites. The information provides input for the development of realistic models that can be used by theory to predict functional properties.

**KEYWORDS:** catalysis, selectivity, oxygen species, operando, AP-XPS, NEXAFS



## INTRODUCTION

The multifaceted compositional and structural chemistry of perovskites turns this mineral class<sup>1</sup> into an attractive experimental ground to explore links between solid-state chemistry and catalysis. The concept has been pursued for a long time.<sup>2,3</sup> Today, advanced experimental and computational methods are available that facilitate descriptor-based identification of potential catalysts for more complex reactions and challenging operating conditions.<sup>4,5</sup>

Pure or partially substituted  $(A,A',A'')(B,B',B'')(O,X)_3$  perovskites have been studied in various catalytic applications,<sup>6,7</sup> including oxygen evolution in alkaline solution,<sup>8</sup> photocatalytic applications,<sup>9</sup> CO oxidation,<sup>10</sup> DeNO<sub>x</sub> reactions,<sup>11</sup> and total combustion of alkanes and volatile organic compounds,<sup>6,12–14</sup> with the aim to replace noble metals as

catalytically active components. Perovskites were implemented in oxygen-permeable membranes used in membrane reactors for selective oxidation of methane and other short-chain alkanes to higher hydrocarbons and olefins.<sup>15–17</sup> Olefins were synthesized at high temperatures over perovskite-supported platinum catalysts in the catalytic partial oxidation of ethane applying short contact times,<sup>18</sup> in catalytic dehydrogenation of propane in the presence of steam,<sup>19,20</sup> and in oxidative

Received: March 19, 2020

Revised: May 29, 2020

Published: May 29, 2020



dehydrogenation of propane applying chemical looping technologies or pulse experiments to control the activation of molecular oxygen on the surface of the perovskite catalyst.<sup>21,22</sup>

The most productive catalysts so far in the activation of short-chain hydrocarbons under oxidative conditions are based on vanadium oxides.<sup>23</sup> In general, high selectivity to value-added products in the oxidation of alkanes is achieved over the semiconductors vanadyl pyrophosphate (VO)<sub>2</sub>P<sub>2</sub>O<sub>7</sub><sup>24</sup> and MoVTenNbO<sub>x</sub><sup>25,26</sup> in *n*-butane or propane oxidation, respectively, even at high alkane conversion. Here, the abundance of highly reactive electrophilic surface oxygen species is controlled by a self-limiting charge carrier transport situation that is created by band bending under the influence of the feed.<sup>27</sup> Thin self-supported layers are formed that contain V<sub>x</sub>O<sub>y</sub> species, which expose the redox-active couple V<sup>4+</sup>/V<sup>5+</sup> and are electronically decoupled from the semiconducting solid. The total combustion catalyst manganese oxide can likewise be converted into a more selective oxidation catalyst by embedding MnO<sub>x</sub> species into a tungsten oxide matrix.<sup>28</sup> MnWO<sub>4</sub> evolves activity and selectivity when a layer of MnO<sub>x</sub> is exposed on the surface that contains a slight excess of the Mn<sup>3+</sup>/Mn<sup>2+</sup> redox couple.

In the present work we question the universality of the hypothesis and investigate whether the selectivity in the oxidative dehydrogenation of propane to propene over Mn perovskites can be changed by surface segregation of manganese oxide species. Different preparation techniques were applied to synthesize AMnO<sub>3</sub> (A = La, Sm) with the aim to explore the potential of this total combustion catalyst in selective oxidation of propane by varying the surface composition. To further evaluate the influence of distortion in Mn-based perovskites, a Sm-deficient perovskite was included. It will be shown that the abundance of Mn on the surface and the presence of steam in the feed determine the selectivity to propene. Changes in the electronic structure of the catalysts at elevated temperature in the reaction environment and the function of various oxygen species that are present on the surface under operation conditions as analyzed by ambient-pressure X-ray photoelectron spectroscopy (AP-XPS) and near-edge X-ray absorption fine structure (NEXAFS) spectroscopy will be discussed.

## ■ EXPERIMENTAL SECTION

**Catalyst Synthesis.** The perovskite catalysts were synthesized via combustion and hydrothermal synthesis.

In the Pechini route,<sup>29</sup> metal nitrates and glycine were used as both complexing agent and fuel, respectively. Ratios between metal nitrates and glycine were calculated, aiming at equal oxygen balance. In the case of LaMnO<sub>3</sub>, 10.78 g of La(NO<sub>3</sub>)<sub>3</sub>·6H<sub>2</sub>O (AlfaAesar), 6.24 g of Mn(NO<sub>3</sub>)<sub>2</sub>·4H<sub>2</sub>O (Merck), and 4.38 g of glycine (Lancaster Synthesis) were dissolved in 35 mL of H<sub>2</sub>O (MilliPore). The clear solution was stirred for 30 min. For the synthesis of SmMnO<sub>3</sub>, 5.01 g of Sm(NO<sub>3</sub>)<sub>3</sub>·6H<sub>2</sub>O (Aldrich) and 3.06 g of Mn(NO<sub>3</sub>)<sub>2</sub>·4H<sub>2</sub>O (ROTH) were dissolved in 40 mL of H<sub>2</sub>O. Then, 2.16 g of glycine (Lancaster Synthesis) was added. The light yellow solution was stirred for 30 min.

The solutions were then quantitatively transferred into an evaporation basin. The solvent was evaporated on a hot plate at 170 °C. Foamlike resins were formed. Using a gas burner, the evaporation basin was heated until the foam started self-ignition. Dark black powders were obtained. LaMnO<sub>3</sub> was used

without further thermal treatment (internal sample ID 24906). SmMnO<sub>3</sub> was calcined in static air at 800 °C for 5 h of heating at 5 °C min<sup>-1</sup> in air (internal sample ID 26849). The catalysts prepared by combustion synthesis are denominated as AMnO<sub>3</sub>-c (A = La, Sm).

For comparison, LaMnO<sub>3</sub> was synthesized via a hydrothermal route,<sup>30,31</sup> by dissolving 18.19 g of La(NO<sub>3</sub>)<sub>3</sub>·6H<sub>2</sub>O (AlfaAesar), 10.54 g of Mn(NO<sub>3</sub>)<sub>2</sub>·4H<sub>2</sub>O (Merck) and 8.82 g of citric acid (Aldrich) in 150 mL of H<sub>2</sub>O in a Teflon-lined autoclave ([La] = 0.28 mol L<sup>-1</sup>). The autoclave was heated at 3 °C min<sup>-1</sup> to 60 °C, and 25 mL of 25% NH<sub>3</sub> solution was added dropwise while stirring. Finally, the pH was increased from 8.7 to 9.0 by adding an additional 9 mL of NH<sub>3</sub> solution. The solution was stirred for 2 h at 60 °C and subsequently heated at 3 °C min<sup>-1</sup> to 140 °C and kept at this temperature for 20 h. After reaction the resulting product was washed three times with H<sub>2</sub>O, separated using a centrifuge, and dried initially at 80 °C and once again at 110 °C. Afterward, 3 g of the powder was calcined for 2 h in a pendulum furnace (Xerion) at 700 °C (heating rate 4 °C min<sup>-1</sup>) in synthetic air, applying a flow of 100 mL min<sup>-1</sup>. The hydrothermally prepared catalyst (internal ID 25104) is denoted as LaMnO<sub>3</sub>-h.

**Catalyst Characterization. X-ray Diffraction.** X-ray diffraction (XRD) patterns were measured on a Bruker D8 ADVANCE II theta/theta diffractometer, using Ni-filtered Cu K $\alpha$  radiation and a position-sensitive LynxEye silicon strip detector. Structure parameters were calculated by least-squares fitting of the diffraction patterns using corresponding structure models taken from the ICSD database. Refinement was performed utilizing the program package TOPAS (version 4.2, copyright 1999–2009 Bruker AXS).

**Chemical Analysis.** The metal content of the perovskite catalysts was determined by X-ray fluorescence spectroscopy using a Bruker S4 Pioneer wavelength dispersive X-ray fluorescence spectrometer. For sample preparation, a mixture of 0.05 g of the catalyst and 8.9 g of lithium tetraborate (>99.995%, Aldrich) was fused into a disk using an automated fusion machine (Vulcan 2 MA, Fluxana). For calibration the binary oxides La<sub>2</sub>O<sub>3</sub>, Sm<sub>2</sub>O<sub>3</sub>, and Mn<sub>3</sub>O<sub>4</sub> were used. Deviations from the ideal stoichiometry of the titer oxides were determined by thermal analysis and taken into account. Oxygen content determination was repeated three times per sample using a TCH600 setup from LECO by applying the inert gas fusion technique. For each measurement, 10 mg of the sample was heated to 3000 °C in a He stream in a graphite crucible. CO and CO<sub>2</sub> formed by reaction of the oxygen in the sample with the crucible were detected by employing an IR cell. Prior to the measurements, the machine was calibrated using Y<sub>2</sub>O<sub>3</sub>.

**Laboratory X-ray Photoelectron Spectroscopy (XPS).** XPS spectra were recorded at room temperature, using non-monochromatized Al K $\alpha$  (1486.6 eV) excitation and a hemispherical analyzer (Phoibos 150, SPECS). The binding energy scale was calibrated by the standard Au 4f<sub>7/2</sub> and Cu 2p<sub>3/2</sub> procedure.

**Surface Area Determination.** N<sub>2</sub> adsorption was performed at -196 °C using the Autosorb-6B analyzer (Quantachrome) after outgassing the catalysts under vacuum for 2 h at 150 °C. All data treatments were performed using the Quantachrome Autosorb software package. The specific surface area was calculated according to the multipoint Brunauer–Emmett–

Teller method (BET) in the range  $0.05 < p/p_0 < 0.15$  assuming a  $N_2$  cross sectional area of  $16.2 \text{ \AA}^2$ .

**Electron Microscopy.** Aberration-corrected scanning transmission electron microscopy (STEM) was performed on a Jeol JEM-ARM200 CF instrument with CEOS CESCOR and CEOS CETCOR hexapole aberration correctors for probe and image-forming lenses, respectively, at 200 kV. STEM images were recorded with a high-angle annular dark-field (HAADF) detector. Prior to the measurements the powdered material was dry-deposited on a holey-carbon-coated copper TEM grid.

Electron energy loss spectrometry (EELS) was performed using a Gatan GIF Quantum image filter. The energy resolution was 0.7 eV, determined at a spectrometer dispersion of 0.1 eV/channel. All spectra were acquired using this dispersion setting utilizing the DualEELS mode, simultaneously recording the low loss spectrum and the core loss spectrum using a drift tube voltage of 510 V, thus showing the O K edge and the Mn  $L_{3,2}$  edge. Simultaneous acquisition of the low-loss spectrum allowed for post-acquisition energy scale corrections. The STEM settings of the microscope were set for a convergence semiangle  $\alpha$  of 20 mrad, while the 5 mm spectrometer entrance aperture led to a collection semiangle  $\beta$  of 46.9 mrad. The acquisition time for the core loss spectra was 10 s per frame, summing three frames. Background subtraction was performed using a 20 eV window for the background fit, starting at 500 eV energy loss. STEM-HAADF images recorded before and after spectrum acquisition were compared to ensure the absence of beam-induced damage or contamination.

**Temperature-Programmed Reduction (TPR).** TPR was performed in a fixed-bed quartz reactor using 30 mg of the catalyst. The TPR measurement was carried out without pretreatment of the catalysts in a mixture of 5.01%  $H_2$  in Ar (flow rate  $30 \text{ mL min}^{-1}$ ), applying a heating rate of  $5 \text{ }^\circ\text{C min}^{-1}$ . The maximum temperature was  $900 \text{ }^\circ\text{C}$ .  $H_2$  consumption was monitored with a thermal conductivity detector.

**Raman Spectroscopy.** Raman spectra were recorded *ex situ* using a customized multiwavelength micro Raman spectroscopy system (S&I Spectroscopy & Imaging GmbH) equipped with a Trivista triple spectrometer (Princeton Instruments) applying only the third stage and corresponding edge filters. Seven laser sources covering from the near-infrared to UV range were adopted. The catalyst was placed on a microscope slide and excited by continuous wave lasers introduced from a microscope objective (10 $\times$ , 15 $\times$ , or 50 $\times$ ). The backscattered light was monitored by a liquid-nitrogen-cooled CCD camera from Princeton Instruments (PyLoN:2K or PyLoN:100, respectively, depending on the laser source used). The primary beam was masked using edge filters. In order to achieve a proper resolution for the respective lasers, the following gratings were used: 300 grooves/mm (633 and 785 nm), 600 grooves/mm (442, 457, 488, and 532 nm) and 2400 grooves/mm (355 nm). To minimize laser damage, the laser power was tuned using two neutral density filters. The detailed measuring conditions (laser power and exposure time) can be found in Table S1 in the Supporting Information.

**Propane Oxidation.** The catalytic tests were carried out using a setup for partial oxidation (Integrated Lab Solutions) with 10 fixed-bed tubular reactors (2 mm inner diameter) in parallel. A detailed description of the experiments and the gas chromatographic analysis is given in the Supporting Information. The conversion of propane,  $X_{C_3H_8}$ , and selectivity

of product  $i$ ,  $S_i$ , in percentages were calculated on the basis of the carbon number and the sum of all products formed

$$X_{C_3H_8} = \frac{\sum_{i=1}^n N_i c_i}{\sum_{i=1}^n N_i c_i + 3c_{C_3H_8, \text{out}}} \times 100$$

$$S_i = \frac{N_i c_i}{\sum_{i=1}^n N_i c_i} \times 100$$

where  $N_i$  is the number of carbon atoms in the product  $i$ ,  $c_i$  is the concentration of the product  $i$  in the reactor exit gas, and  $c_{C_3H_8, \text{out}}$  is the concentration of propane in the exit gas. The carbon balance

$$\text{carbon balance} = \frac{\sum_{i=1}^n N_i c_i + 3c_{C_3H_8, \text{out}}}{3c_{C_3H_8, \text{in}}} \times 100$$

where  $c_{C_3H_8, \text{in}}$  is the concentration of propane in the reactant gas varies between 99.7% and 102% in all experiments. The conversion of oxygen was calculated on the basis of the difference in the oxygen concentration of reactant feed  $C_{O_2, \text{in}}$  and exit gas  $C_{O_2, \text{out}}$ :

$$X_{O_2} = \frac{c_{O_2, \text{in}} - c_{O_2, \text{out}}}{c_{O_2, \text{in}}} \times 100$$

Integral reaction rates  $r_{\text{propane}}$  normalized to the specific surface area in  $\mu\text{mol h}^{-1} \text{ m}^{-2}$  for propane consumption were determined on the basis of the first derivation of the linear function  $X_{C_3H_8} = f\left(\frac{W}{F}\right)$ :

$$r_{\text{propane}} = \frac{dX_{C_3H_8}}{d\left(\frac{W}{F}\right)S}$$

where  $X_{C_3H_8}$  is used not as a percentage but as a value between 0 and 1,  $W$  is the catalyst mass in g,  $F$  is the flow rate of propane in  $\mu\text{mol h}^{-1}$ , and  $S$  is the specific surface area in  $\text{m}^2 \text{ g}^{-1}$ .

**Ambient-Pressure X-ray Photoelectron Spectroscopy (AP-XPS).** Ambient-pressure X-ray photoelectron spectroscopy measurements were performed at the ISSS (Innovative Station for In Situ Spectroscopy) facility at the synchrotron radiation source BESSY II in Berlin, Germany. The beamline was described in previous publications.<sup>32,33</sup> Measurement parameters and data analysis are explained in the Supporting Information.

A pressed pellet of 13 mg of the perovskite powder was measured first at room temperature under vacuum and then heated in a 0/20/80/0 propane/ $O_2$ /He/ $H_2O$  mixture (heating rate  $5 \text{ }^\circ\text{C min}^{-1}$ ) to  $270 \text{ }^\circ\text{C}$ . All gases and water vapor were dosed to the XPS cell via calibrated mass flow controllers (BRONKHORST). The gas composition was then switched consecutively to 0/5/95/0, 10/5/85/0, 5/10/85/0, and 5/10/45/40, back to 0/5/95/0, and finally to 10/5/85/0. The total gas pressure under all reaction conditions was 25 Pa. The gas-phase composition was monitored using a VARIAN CP-4900 micro gas chromatograph (micro-GC) and an IONICON proton-transfer-reaction mass spectrometer (PTR-MS).

**In Situ Near-Edge X-ray Absorption Fine Structure (NEXAFS) Spectroscopy.** NEXAFS was conducted at the Mn  $L_{3,2}$  edges in the AP-XPS cell under the conditions applied in AP-XPS by moving the monochromator continuously with a

speed of 0.23 eV s<sup>-1</sup>. The exit slit of the beamline was 111 μm for all measurements. The lens housing of the AP-XPS spectrometer was biased with +90 V and used as a Faraday cup to collect the NEXAFS in the total electron yield mode (TEY). A linear background has been subtracted, and the edge jump intensity has been normalized at 660 eV. The NEXAFS has been analyzed by determining the contribution of Mn<sup>2+</sup>, Mn<sup>3+</sup>, and Mn<sup>4+</sup> species, by a linear combination of reference spectra for the single Mn oxidation states.

## RESULTS AND DISCUSSION

**Bulk and Nanostructure of the Mn-Based Perovskite Catalysts.** According to X-ray diffraction, the perovskites are phase-pure (Table 1). Both LaMnO<sub>3</sub>-c and LaMnO<sub>3</sub>-h show

**Table 1. Specific Surface Area and Structural Characteristics of Calcined and Spent Catalysts**

	calcined catalysts		
	LaMnO <sub>3</sub> -h	LaMnO <sub>3</sub> -c	SmMnO <sub>3</sub> -c
S (m <sup>2</sup> g <sup>-1</sup> )	34.1	29.2	6.9
space group	R $\bar{3}c$	R $\bar{3}c$	<i>Pnma</i>
lattice parameters (Å)			
<i>a</i>	5.49745(18)	5.524(3)	5.82205(16)
<i>b</i>			7.5015(2)
<i>c</i>	13.3017(7)	13.547(15)	5.36391(16)
cell volume (Å <sup>3</sup> )	348.15(3)	357.4(6)	234.265(11)
crystallite size Vol-IB (nm)	43.6(8)	49.9(14)	59.8(7)
strain (%)	0.1815(15)	0.2938(17)	0.1098(9)
	spent catalysts		
	LaMnO <sub>3</sub> -h	LaMnO <sub>3</sub> -c	SmMnO <sub>3</sub> -c
space group	R $\bar{3}c$	R $\bar{3}c$	<i>Pnma</i>
lattice params			
<i>a</i>	5.49835(17)	5.5193(4)	5.81905(19)
<i>b</i>			7.4944(2)
<i>c</i>	13.3014(7)	13.4197(18)	5.36003(18)
cell volume (Å <sup>3</sup> )	348.25(3)	354.04(7)	233.752(13)
crystallite size Vol-IB (nm)	38.1(5)	29.5(8)	67.2(2)
strain (%)	0.1677(15)	0.208(6)	0.138(2)

diffraction patterns that correspond exclusively to the rhombohedral perovskite structure (ICSD #75216) (Figure

S1). The cell volume of LaMnO<sub>3</sub>-c is slightly increased in comparison to that of LaMnO<sub>3</sub>-h, indicating more oxygen defects in LaMnO<sub>3</sub>-c in comparison to LaMnO<sub>3</sub>-h.<sup>34–37</sup> The smaller ionic radius of Sm<sup>3+</sup> in comparison to La<sup>3+</sup> forces the SmMnO<sub>3</sub>-c to crystallize in the orthorhombic perovskite structure (ICSD #95491) (Figure S1). However, the structural motif of Jahn–Teller-distorted [Mn<sup>III</sup>O<sub>6</sub>] octahedra is maintained in all three catalysts. Only the degree of tilting of these octahedra increases with decreasing rare-earth-metal ion radius: i.e., by going from the rhombohedral (A = La) to the orthorhombic structure (A = Sm).

The B/A ratio in the bulk of the perovskites depends on both the synthesis technique and amounts of reactants (Table 2). LaMnO<sub>3</sub>-h exhibits a distinct excess of La<sup>3+</sup> in the bulk. Oxygen excess reflected in δ > 0 for La<sub>x</sub>MnO<sub>3+δ</sub> (Table 2) is a general property of the La-Mn perovskites under investigation. The nonstoichiometry with regard to oxygen has been attributed to Mn cation vacancies.<sup>36,37</sup> The combustion synthesis allows for enrichment of Mn in the bulk by using an excess of the Mn source in the synthesis (nominal composition in Table 2), which results in a better utilization of the phase width of Mn-based perovskites.<sup>38,39</sup> Mn<sup>3+</sup> ions occupy vacant La<sup>3+</sup> positions to enable a balanced structure.<sup>40</sup> The variability of the Mn oxidation state (II, III, IV) buffers forbidden charging and thus guarantees charge neutrality in the Mn-based perovskites for different chemical compositions. To summarize, an excess and a deficiency of La<sup>3+</sup> is balanced by the formation of manganese and oxygen vacancies, respectively.<sup>41</sup>

High-angle annular dark-field scanning transmission electron microscopy (HAADF-STEM) imaging reveals crystalline particles for all investigated catalysts (Figure 1 and Figures S2–S4). Nanoscale, crystalline by-phase oxides were not identified. STEM imaging of the surface termination under vacuum suggests that the investigated perovskite catalysts contain surface terminations that are enriched in La (LaMnO<sub>3</sub>-c, Figure 1a; LaMnO<sub>3</sub>-h, Figure S3a), Mn (LaMnO<sub>3</sub>-c, Figure 1b; LaMnO<sub>3</sub>-h, Figure S3b; SmMnO<sub>3</sub>-c, Figure S4a), or Sm (SmMnO<sub>3</sub>-c, Figure S4a,b). Mn cations that are slightly displaced from their ideal equilibrium position toward the vacuum have also been observed at the surface of LaMnO<sub>3</sub>-c (Figure 1b).

**Table 2. Chemical Composition and Mn Oxidation State Determined by Different Techniques**

	catalyst		
	LaMnO <sub>3</sub> -h	LaMnO <sub>3</sub> -c	SmMnO <sub>3</sub> -c
nominal composition	LaMnO <sub>3</sub>	LaMnO <sub>3</sub>	Sm <sub>0.96</sub> MnO <sub>3</sub>
bulk B/A atomic ratio <sup>a</sup>	0.79	1.01	1.04
O content (wt %) <sup>b</sup>	20.39 ± 0.48	23.23 ± 0.13	18.16 ± 0.12
chemical composition <sup>c</sup>	La <sub>1.12</sub> Mn <sub>0.88</sub> O <sub>3.26</sub>	La <sub>0.99</sub> Mn <sub>1.00</sub> O <sub>3.66</sub>	Sm <sub>0.98</sub> Mn <sub>1.02</sub> O <sub>2.81</sub>
all elements normalized to B <sup>c</sup>	La <sub>1.27</sub> MnO <sub>3.70</sub>	La <sub>1.01</sub> MnO <sub>3.69</sub>	Sm <sub>0.96</sub> MnO <sub>2.75</sub>
δ in A <sub>x</sub> BO <sub>3+δ</sub>	+0.70	+0.69	-0.25
Mn oxidation state (La, 3+; O, 2-) <sup>c</sup>	3.57	4.36	2.71
Mn oxidation state (XPS) <sup>d</sup>	3.41	3.1	2.7
Mn oxidation state (NEXAFS) <sup>e</sup>	4.0	3.24	3.06
Mn oxidation state (TPR/XRF) <sup>f</sup>	3.32	3.23	2.93

<sup>a</sup>According to metal determination using X-ray fluorescence analysis; no information on O content. <sup>b</sup>According to oxygen analysis based on inert gas fusion technique; no information on A and B content. <sup>c</sup>Calculated on the basis of the combined chemical analysis of metals (footnote a) and oxygen (footnote b). <sup>d</sup>Determined on the basis of Mn 3s splitting. <sup>e</sup>Determined on the basis of Mn L<sub>3,2</sub> edge fitting. <sup>f</sup>Determined on the basis of temperature-programmed reduction assuming the XRF-based formula A<sub>x</sub>BO<sub>3</sub> (0.96 < x < 1.27).

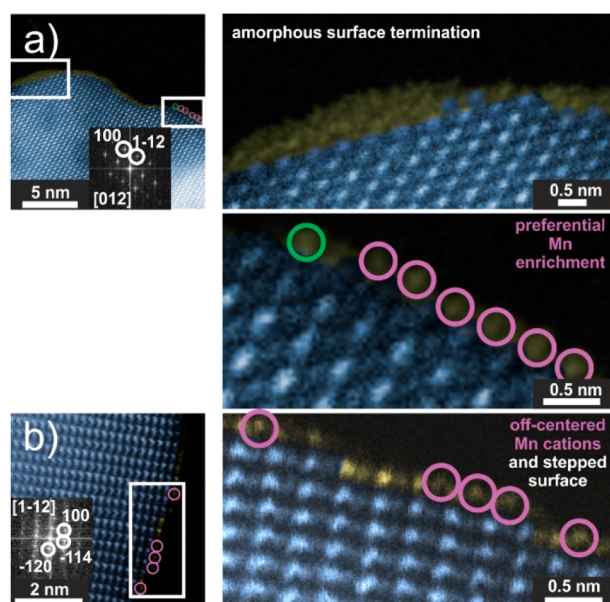


**Figure 1.** HAADF-STEM images of  $\text{LaMnO}_3\text{-c}$ : (a, b) high-resolution HAADF-STEM images of different  $\text{LaMnO}_3$  crystals. The insets show FFTs of the images. On the right are magnified surface terminations taken from the regions of interest highlighted in the left HAADF-STEM images (white boxes in (a) and (b)). The magnified region of (b) was rotated counterclockwise by  $90^\circ$ . The false colors highlight bulk (blue) and surface regions (yellow); green circles denote La surface sites, while pink circles show Mn surface centers. Original images are presented in Figure S2 in the Supporting Information.

The HAADF-STEM images also suggest the presence of structurally decoupled (Figure S3c) and amorphous surface layers (Figure 1a and and Figure S4b).  $\text{LaMnO}_3\text{-h}$ , in particular, shows particles which are terminated entirely by La atoms (Figure S3a), indicated by bright spots and agreeing well with the increased La content in the bulk found by XRF (Table 2). However, also Mn-terminated surfaces have been found on the surface of the same catalyst (Figure S3b). The HAADF-STEM images of  $\text{LaMnO}_3\text{-c}$  (Figure 1) and  $\text{SmMnO}_3\text{-c}$  (Figure S4) also show stepped surfaces with slightly displaced Mn or Sm atom columns.  $[\text{MnO}_6]$  octahedra as surface termination units are highly irregular, showing an elongated Mn–O bond pointing into the free room, while the diametric Mn–O bond is shortened with respect to the bulk Mn–O bonds. In addition, the ability of Mn ions to occupy the 12-fold-coordinated position of La ions leads to probably irregular  $\text{MnO}_x$  species on the surface.

La-site deficiency and partial substitution of A sites with Mn in oxidation state 2+ can lead to the coexistence of  $\text{Mn}^{3+}$  and  $\text{Mn}^{2+}$  redox couples on the surface of  $\text{LaMnO}_3$ , as has been shown by high-energy resolution electron energy loss spectroscopy for a material that was applied as an electrode in the oxygen reduction reaction.<sup>42</sup> Figure 2 shows a comparison of the Mn  $L_{3,2}$  energy loss near-edge structure (ELNES) in the bulk and on the surface of  $\text{SmMnO}_3\text{-c}$ . The main peak of the  $L_3$  edge is shifted by 1.5 eV, indicating strong contributions of  $\text{Mn}^{2+}$  species on the surface and mainly  $\text{Mn}^{3+}$  species in the bulk of the investigated particle. In the bulk spectrum less contribution of  $\text{Mn}^{2+}$  is expected because the beam is irradiating not only the surface region but also dominantly the bulk region. On the basis of the inelastic mean free path (IMFP), the surface ELNES gives information on about 22

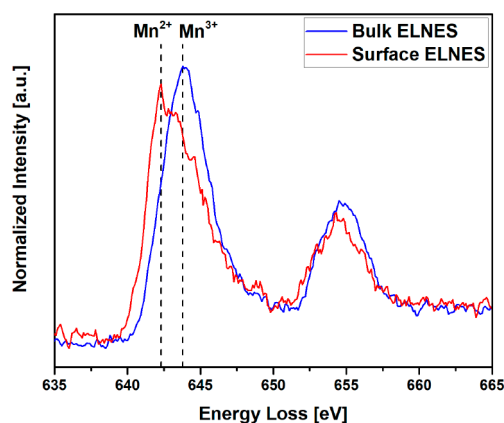


**Figure 2.** Mn  $L_{3,2}$  ELNES acquired in the bulk and on the surface of a  $\text{SmMnO}_3\text{-c}$  particle. It can be seen that the surface spectrum shows a strong contribution of  $\text{Mn}^{2+}$  species in comparison to the  $\text{Mn}^{3+}$  species dominated bulk spectrum. This is evident from the 1.5 eV energy shift of the main peak of the  $L_3$  edge and changes in the shape of the peak.

unit cells (estimated particle thickness 11 nm, IMFP = 0.13), mainly located on the surface, and the bulk ELNES gives information on about 60 unit cells (estimated particle thickness 30 nm, IMFP = 0.35), mainly located in the bulk, which is also indicated by the measured total intensity (Figure S5). Thus, the  $\text{Mn}^{2+}$  is enriched in the surface region and the small contribution of  $\text{Mn}^{2+}$  in the bulk ELNES is ascribed to the surface scanned inevitably during the bulk ELNES scan. The full spectrum including the O K edge is shown in Figure S5, while the STEM-HAADF image with indications of the acquisition position of the energy loss spectra can be seen in Figure S6. These EELS measurements were repeated on several nanoparticles, giving similar results. However, on some  $\text{SmMnO}_3\text{-c}$  nanoparticles there were no differences in bulk and surface spectra visible. This indicates the presence of different surface terminations.

In summary, electron microscopy suggests that the catalyst particles show diverse terminations by both A and B, as well as irregularly structured overlayers. The predominant oxidation state of Mn on the surface of  $\text{SmMnO}_3\text{-c}$  is 2+. The investigation excludes considerable segregation of binary oxide nanoparticles.

Multiwavelength Raman spectroscopy has been used to further study the structural disorder of the catalysts (Figure 3). The Raman spectra measured at room temperature by using an excitation laser of 633 nm (1.96 eV) are in good agreement with the literature.<sup>43,44</sup> According to lattice dynamic calculations, five modes ( $A_{1g}$  and 4  $E_g$ ) are Raman-allowed for the ideal rhombohedral structure.<sup>44</sup> In the spectrum of  $\text{LaMnO}_3\text{-c}$  (Figure 3,  $\lambda_{\text{ex}} = 633$  nm) three dominant bands are observed at 236, 495, and 616  $\text{cm}^{-1}$ . The peak at 236  $\text{cm}^{-1}$  can be assigned to a rotational  $A_{1g}$  mode. The other two peaks correspond to bending and stretching Mn–O vibrations, respectively, but are, according to the literature, not in accurate agreement with the expected  $E_g$  modes of the ideal rhombohedral crystal structure.<sup>44</sup>

Deviations are common in spectra of mixed-valence manganites and are caused by variations in the metal site occupancy and the oxidation state of manganese.<sup>45</sup> The  $\text{Mn}^{3+}/\text{Mn}^{4+}$  ratio affects the Raman spectra due to differences in the local symmetry, since  $[\text{Mn}^{\text{III}}\text{O}_6]$  octahedra exhibit stretching

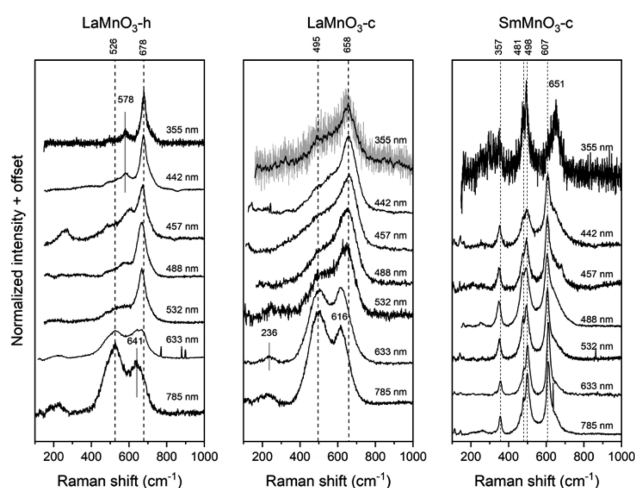


**Figure 3.** *Ex situ* Raman spectra of LaMnO<sub>3</sub>-h (left), LaMnO<sub>3</sub>-c (middle), and SmMnO<sub>3</sub>-c (right) recorded using different excitation wavelength lasers (see Table S1). Spectra are shown with offsets for better comparison after background subtraction and intensity normalization at 678 cm<sup>-1</sup> for LaMnO<sub>3</sub>-h, 658 cm<sup>-1</sup> for LaMnO<sub>3</sub>-c, and 607 cm<sup>-1</sup> for SmMnO<sub>3</sub>-c.

distortions due to the Jahn–Teller effect. The effect does not occur in [Mn<sup>IV</sup>O<sub>6</sub>] octahedra. The random distribution of Mn<sup>3+</sup> and Mn<sup>4+</sup> results in locally distorted oxygen sublattices. Therefore, the Raman spectrum of rhombohedral LaMnO<sub>3</sub> is dominated by disorder-induced bands.<sup>45</sup> Consequently, the different preparation techniques of the two rhombohedral catalysts LaMnO<sub>3</sub>-c and LaMnO<sub>3</sub>-h are reflected in differences in the peak maxima (Figure 3). The shift to higher wavenumbers (526 and 641 cm<sup>-1</sup>) in LaMnO<sub>3</sub>-h is also in agreement with the decreased cell volume of the hydrothermally prepared catalyst (Table 1). The broadening of the peaks has been attributed to a larger deviation of the real structure from the ideal structure, most likely due to different extents of oxygen excess,<sup>45</sup> which is in agreement with XRD and oxygen analysis (Tables 1 and 2). Broadening due to laser annealing is minimized in the present experiment, since the employed laser powers should not affect the rhombohedral structure (Table S1).<sup>43</sup>

The orthorhombic *Pnma* structure gives rise to 24 allowed Raman modes (7A<sub>g</sub>, 5B<sub>1g</sub>, 7B<sub>2g</sub>, and 5B<sub>3g</sub>).<sup>44</sup> The most prominent bands observed in the spectrum of SmMnO<sub>3</sub>-c (Figure 3) are located at 357, 481, 498, and 607 cm<sup>-1</sup>. The peaks are tentatively attributed to B<sub>3g</sub> rotation, B<sub>2g</sub> out-of-phase bending, A<sub>g</sub> out-of-phase bending, and B<sub>2g</sub> in-phase stretching modes, respectively. Since the Jahn–Teller distortion is compatible with the orthorhombic structure, the effect does not contribute to the appearance of disorder-induced peaks in the spectrum and the bands are comparatively narrow.<sup>43</sup>

The spectra change significantly by using higher excitation energies. Here, laser wavelengths of 532, 488, 457, 442, and 355 nm (2.3, 2.5, 2.7, 2.8, and 3.5 eV) were applied (Figure 3). The results are in agreement with the resonant behavior of the phonon Raman cross section in LaMnO<sub>3</sub> when the excitation energy is close to the Jahn–Teller gap at 2 eV.<sup>46</sup> When higher excitation energies are used, additional bands are detected at 578 cm<sup>-1</sup> and 678 cm<sup>-1</sup> in LaMnO<sub>3</sub>-h, 658 cm<sup>-1</sup> in LaMnO<sub>3</sub>-c, and 651 cm<sup>-1</sup> in SmMnO<sub>3</sub>-c (Figure 3). A weak line at 653 cm<sup>-1</sup> was attributed to defects in YMnO<sub>3</sub>.<sup>43</sup> Recently, a strong wavelength dependence was observed for the Raman spectra of

nanostructured MnWO<sub>4</sub> catalysts that exhibit extraframework MnO<sub>x</sub> surface chains showing bands centered at 620 and 665 cm<sup>-1</sup>.<sup>47</sup> The feature at 651 cm<sup>-1</sup> in the spectrum of SmMnO<sub>3</sub>-c, and perhaps also the peaks at 678 cm<sup>-1</sup> in LaMnO<sub>3</sub>-h and 658 cm<sup>-1</sup> in LaMnO<sub>3</sub>-c, might, therefore, also indicate the presence of segregated manganese oxide surface species.<sup>48</sup> Such an assignment would be in agreement with the detection of Mn oxide single and double layers by electron microscopy (Figure 1 and Figures S2–S4).

In summary, Raman spectroscopy reveals a high degree of disorder in the catalysts with a rhombohedral crystal structure. In addition, evidence for segregation of MnO<sub>x</sub> surface species, in particular on the surface of SmMnO<sub>3</sub>-c, is provided.

**Catalytic Performance in Oxidative Dehydrogenation of Propane.** The catalysts exhibit high activity in the oxidative dehydrogenation of propane with an onset of the reaction at temperatures already below 230 °C (Figure 4, Figure S7, and

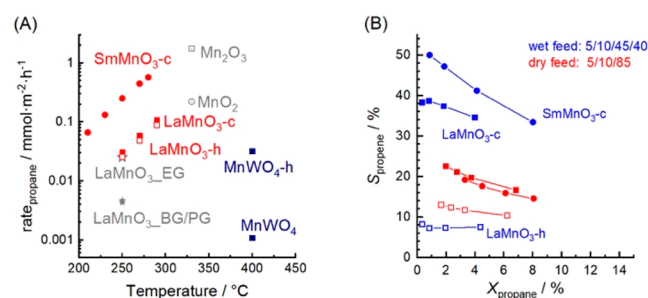


**Figure 4.** (A) Rates of propane consumption over LaMnO<sub>3</sub>-c (filled squares), SmMnO<sub>3</sub>-c (filled circles), and LaMnO<sub>3</sub>-h (open squares) in the oxidative dehydrogenation of propane in a feed of 10/5/85 propane/O<sub>2</sub>/N<sub>2</sub> (W/F = 0.2 g s mL<sup>-1</sup>) as a function of temperature. Rates of MnWO<sub>4</sub>, Mn<sub>2</sub>O<sub>3</sub>, and MnO<sub>2</sub><sup>28</sup> as well as LaMnO<sub>3</sub>\_EG, LaMnO<sub>3</sub>\_BG, and LaMnO<sub>3</sub>\_PG<sup>49</sup> (h, hydrothermal; EG, 1,2-ethylene glycol; BG, 1,4-butylene glycol; PG, 1,3-propylene glycol) are taken from the literature. (B) Selectivity to propene as a function of the temperature range between 250 and 310 °C (W/F = 0.2 g s mL<sup>-1</sup>) in a dry, oxygen-rich feed (5/10/85/0 propane/O<sub>2</sub>/N<sub>2</sub>/H<sub>2</sub>O (red)) and wet, oxygen-rich feed (5/10/45/40 propane/O<sub>2</sub>/N<sub>2</sub>/H<sub>2</sub>O (blue)).

Table 3). LaMnO<sub>3</sub>-c and LaMnO<sub>3</sub>-h show similar and SmMnO<sub>3</sub>-c higher specific reaction rates (normalized to the specific surface area of the catalyst) in comparison to LaMnO<sub>3</sub> that has been applied in the total combustion of propane and tested in a high excess of air in the feed.<sup>49</sup> Increasing the oxygen to propane ratio results in increased propane conversion, showing the effect of the oxygen partial pressure on the overall reaction rate (Figure S7). The rates are comparable to rates measured over the total combustion catalysts Mn<sub>2</sub>O<sub>3</sub> and MnO<sub>2</sub> and much higher in comparison to nanostructured MnWO<sub>4</sub> that also exhibits an enrichment of MnO<sub>x</sub> on the surface.<sup>28</sup> The activity trend scales with the onset of hydrogen consumption in temperature-programmed reduction (Figure S8). The two LaMnO<sub>3</sub> catalysts are similar in terms of activity and onset temperature in H<sub>2</sub>-TPR (160 °C), whereas a lower onset temperature of 130 °C was measured for the more active SmMnO<sub>3</sub>-c catalyst. However, the apparent activation energy is similar for all catalysts under oxygen-poor and oxygen-rich feed compositions (Table 3), suggesting a similar nature of the active phase. In addition to CO<sub>2</sub>, propene is formed as a second product (Figure 4B) with a selectivity of approximately 20% for the catalysts prepared by combustion

**Table 3. Propane Consumption Rates at 270 °C and Apparent Activation Energies  $E_a$  (250 °C <  $T$  < 310 °C, W/F = 0.2 g s mL<sup>-1</sup>) in Dry Feed (Propane/O<sub>2</sub>/N<sub>2</sub>/H<sub>2</sub>O = 10/5/85/0), Dry, Oxygen-Rich Feed (Propane/O<sub>2</sub>/N<sub>2</sub>/H<sub>2</sub>O = 5/10/85/0), and Wet, Oxygen-Rich Feed (Propane/O<sub>2</sub>/N<sub>2</sub>/H<sub>2</sub>O = 5/10/85/40)**

	LaMnO <sub>3</sub> -h	LaMnO <sub>3</sub> -c	SmMnO <sub>3</sub> -c
$r_{\text{propane\_dry}}$ ( $\mu\text{mol h}^{-1} \text{m}^{-2}$ )	56.1 ± 2.6	73.8 ± 3.4	500 ± 23
$r_{\text{propane\_dryOrich}}$ ( $\mu\text{mol h}^{-1} \text{m}^{-2}$ )	38.9 ± 1.8	51.1 ± 2.3	349 ± 16
$r_{\text{propane\_wet}}$ ( $\mu\text{mol h}^{-1} \text{m}^{-2}$ )	9.9 ± 0.5	10.9 ± 0.5	106.9 ± 4.9
$E_{a\text{-dry}}$ (kJ mol <sup>-1</sup> )	77 ± 0.3	77 ± 0.2	70 ± 0.6
$E_{a\text{-dryOrich}}$ (kJ mol <sup>-1</sup> )	82 ± 0.4	77 ± 0.4	73 ± 0.6
$E_{a\text{-wet}}$ (kJ mol <sup>-1</sup> )	110 ± 0.3	106 ± 0.7	96 ± 1.3

synthesis and even lower selectivity for the hydrothermally derived catalyst. Possibly formed CO is likely fully converted to CO<sub>2</sub>,<sup>10,50,51</sup> which is different in comparison to V-based catalysts applied in the oxidative dehydrogenation of propane.<sup>52,53</sup> No oxygenates were observed. The selectivity decreases further at higher temperatures at which V-based catalysts are normally studied (Figure S9); however, the drop is quite moderate, suggesting that consecutive reactions of propene are less important over perovskites. Variation of the oxygen content in the feed has no effect on the selectivity (Figure S10).

The selectivity to propene is significantly increased by adding H<sub>2</sub>O to the oxygen-rich feed, in particular for SmMnO<sub>3</sub>-c. The increase is less distinct for LaMnO<sub>3</sub>-c (Figure 4B). In contrast, the LaMnO<sub>3</sub>-h catalyst shows decreased selectivity to propene on employing a wet feed. The cofed H<sub>2</sub>O decreases the conversion of propane slightly.<sup>54</sup> Water may block a part of the adsorption sites, since strong interaction between H<sub>2</sub>O and ideal Mn-terminated perovskites has been reported.<sup>55</sup> Alternatively, water in the feed may change the concentration of adsorbed oxygen species by shifting the equilibrium of catalyst regeneration reactions.<sup>56</sup> In any case, the selectivity increase is not caused by decreased conversion (Figure 4B). The apparent activation energy increases for all catalysts including LaMnO<sub>3</sub>-h, which shows reduced selectivity in a wet feed (Table 3). Irrespective of the differing catalytic behaviors of the three catalysts, their crystalline structures (Figures S11 and S12) as well as their surface compositions (Table S2) remained stable during catalytic testing in dry and wet feeds. LaMnO<sub>3</sub>-c showed some decrease in cell volume after catalysis (Table 1), indicating healing of oxygen vacancies under reaction conditions.<sup>34</sup> The changes in the lattice volume of SmMnO<sub>3</sub>-c are smaller (Table 1). According to the lattice parameters of the spent LaMnO<sub>3</sub>-h, no changes in the bulk are found in this case. The stability of the bulk crystal structure is also demonstrated by the HAADF-STEM images of the spent LaMnO<sub>3</sub> catalysts (Figure S12).

#### Surface Characterization of the Working Catalysts.

Ambient-pressure XPS reveals differences in the elemental composition near the surface in comparison to the bulk concentration, which was determined by X-ray fluorescence (Figure 5). The SmMnO<sub>3</sub>-c catalyst exhibits a slightly higher Mn concentration on the surface of the fresh catalysts. The La-containing catalysts, in particular LaMnO<sub>3</sub>-h, are characterized by a shortage of surface Mn. No significant changes are observed under the different reaction conditions. The distribution of surface oxygen species as well as the oxidation state of manganese, however, undergo considerable changes, especially in a switch from dry to wet feed.

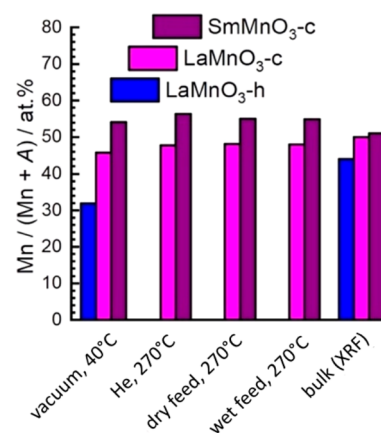


**Figure 5.** Fraction of Mn related to the metal content in the bulk (XRF) and in the near-surface region (IMFP = 0.6 nm), calculated from AP-XPS spectra. Applied conditions are given below the  $x$  axis. LaMnO<sub>3</sub>-h was only measured at room temperature under vacuum. The total pressure was constant at 25 Pa employing all feeds.

The nature of the oxygen surface species, which are responsible for the activation of the reacting molecules, was analyzed by fitting the O 1s core level spectra of LaMnO<sub>3</sub>-c and SmMnO<sub>3</sub>-c (Figure 6 and Table 4), which requires the contribution of seven different oxygen species. The fitting procedure is described in detail in the Supporting Information. Differentiation and assignment of the components were derived from the development of the O 1s peak during variation of temperature (Figures S13 and S14), feed composition, and excitation energy (Figure 7 and Figure S15). The assignment is discussed with regard to the literature.<sup>57–59</sup> Fitting parameters<sup>60</sup> are summarized in Table 4.

The O<sub>lattice</sub> peak occurs at the lowest binding energy of 529.2 eV. It originates from regular lattice oxygen atoms and, thus, increases in intensity if higher excitation energies are used, which extends the inelastic mean free path (IMFP) of the electrons and consequently the information depth (Figure 7 and Figure S15, white squares).<sup>57,58,61,62</sup>

The peak at 530.1 eV is assigned to oxygen atoms positioned next to defects (O<sub>defect</sub>).<sup>57,62</sup> In contrast to O<sub>lattice</sub>, the contribution of O<sub>defect</sub> decreases when higher excitation energies are used, showing that the corresponding O<sub>defect</sub> sites are more abundant in the near-surface region (Figure 7 and Figure S15, compare white and black squares). The remarkable fraction of defects is in line with calculations suggesting a stabilization of the (001) and (110) surfaces of LaMnO<sub>3</sub> by oxygen vacancies.<sup>63,64</sup> These defect-related oxygen atoms may, however, also be located next to cation vacancies,

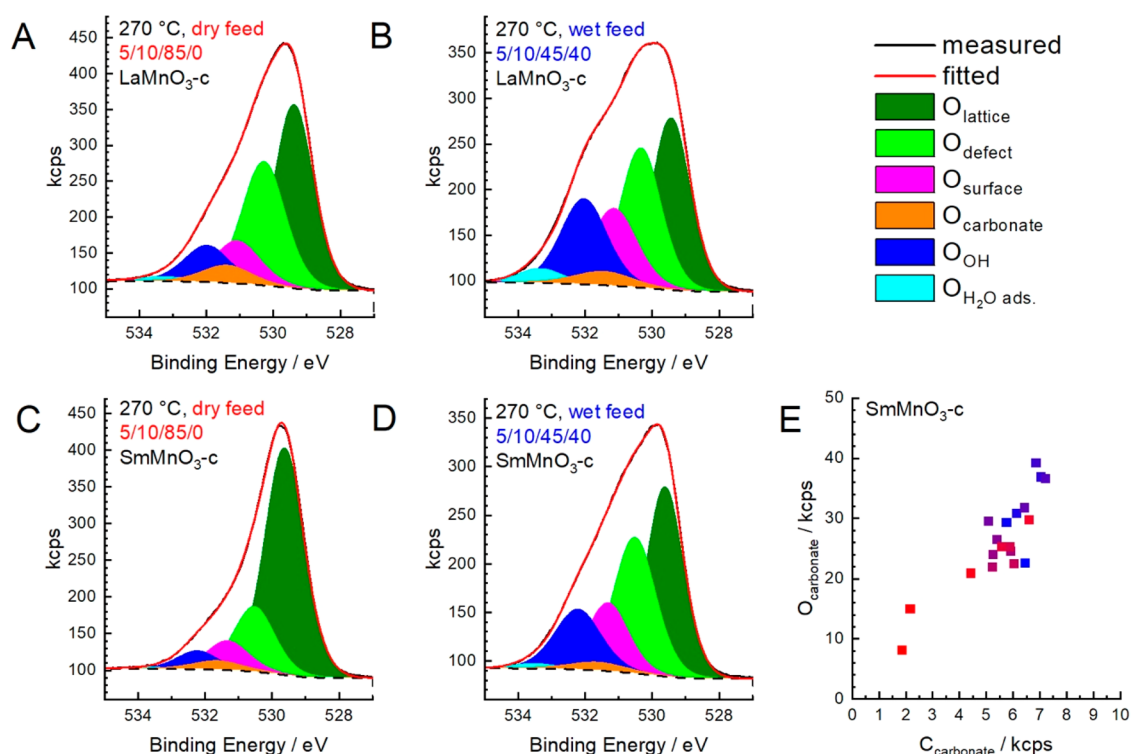


**Figure 6.** Measured O 1s spectra (black) collected at 270 °C for LaMnO<sub>3</sub>-c in a dry (A) and wet propane oxidation feed (B) as well as SmMnO<sub>3</sub>-c in a dry (C) and wet (D) feed (feed composition indicated in the figures as propane/O<sub>2</sub>/He/H<sub>2</sub>O ratios) and the corresponding fits (red) using seven single contributions (colored peaks with the assignment provided in the legend). The broken line represents the background. (E) Correlation of the intensity of the O 1s peak due to O<sub>carbonate</sub> as a function of the C 1s peak of C<sub>carbonate</sub> during heating from room temperature to 270 °C (the temperature is illustrated by using a color code from blue (room temperature) to red (270 °C)) in 20% O<sub>2</sub> (Figure S13).

**Table 4. Summary of Fit Parameters Used for O 1s Spectral Fitting<sup>a</sup>**

	oxygen species						
	O <sub>lattice</sub>	O <sub>defect</sub>	O <sub>surface</sub>	O <sub>carbonate</sub>	O <sub>OH</sub>	O <sub>H<sub>2</sub>O ads.</sub>	O <sub>oxygenates ads.</sub>
BE (eV)	529.2	530.1	530.9	531.2	531.8	533.2	534–535
fwhm (eV)	1.1–1.3	1.4–1.6	1.4–1.6	1.7–2.0	1.4–1.6	1.5–1.7	1.5–1.7

<sup>a</sup>The Gaussian–Lorentzian mixing factor was used as defined in CASA XPS.<sup>60</sup> The absolute binding energy (BE) accuracy is estimated to be around ±0.1 eV.

frequently present in Mn-based perovskites.<sup>36,37,41</sup> The O<sub>defect</sub> signal increases slightly during heating in 20% O<sub>2</sub> in helium at temperatures above 150 °C (Figure S14) and further in a dry propane oxidation feed, whereas it decreases slightly again in a wet feed on LaMnO<sub>3</sub>-c (Figure 7). The limited data of the measurement of SmMnO<sub>3</sub>-c exhibit a constant O<sub>defect</sub> concentration and even an increase in wet feed (Figure S15). In conclusion, the experiments under different atmospheres support that oxygen vacancies cause the shift in binding energy in comparison to regular bulk oxygen atoms.

The peak at 530.9 eV decreases due to evacuation ( $1 \times 10^{-5}$  Pa) at 40 °C and further during the pretreatment in 20% O<sub>2</sub> in He (Figure S14). The signal reaches a very low intensity level already at a temperature of 100 °C. A slight increase is observed again in the propane oxidation feed at 270 °C and in particular when steam is added (Figure 7 and Figure S15). On the basis of the very low temperature at which the peak disappears, its origin is tentatively attributed to surface or adsorbed oxygen species, for example O<sup>-</sup>, on the surface of the perovskites, which is also in accordance with the literature.<sup>57–59,65</sup> Consequently, the peak at 530.9 eV is called O<sub>surface</sub>. The measurement of LaMnO<sub>3</sub>-c at the reaction

temperature (Figure 7), which contains more data points in comparison to the measurement of SmMnO<sub>3</sub>-c (Figure S15), suggests that the trend of O<sub>surface</sub> mirrors the trend of O<sub>defect</sub> to some extent: i.e., O<sub>surface</sub> increases when O<sub>defect</sub> decreases. The observation is in agreement with the assumption that the creation of oxygen vacancies in a propane-containing feed at elevated temperature provides active sites for oxygen adsorption and dissociation.<sup>66,67</sup> The measured data points probe steady-state situations that result from such processes.

The formation of surface carbonate species was monitored in a separate CO<sub>2</sub> adsorption experiment. After pretreatment of SmMnO<sub>3</sub>-c in 20% O<sub>2</sub> balanced by He from room temperature to 270 °C, CO<sub>2</sub> was fed and the catalyst was cooled in flowing CO<sub>2</sub> to room temperature again. The O<sub>carbonate</sub> peak is identified at a binding energy of 531.2 eV, which increases to the same extent as the C<sub>carbonate</sub> peak increases. The C 1s binding energies appear between 288 and 289 eV (Figure S16). In all temperature-programmed desorption experiments, the O<sub>carbonate</sub> intensity (Figure S17) was calculated on the basis of the C<sub>carbonate</sub> intensity (Figure S16), and the intensity ratio was kept constant in all fits.

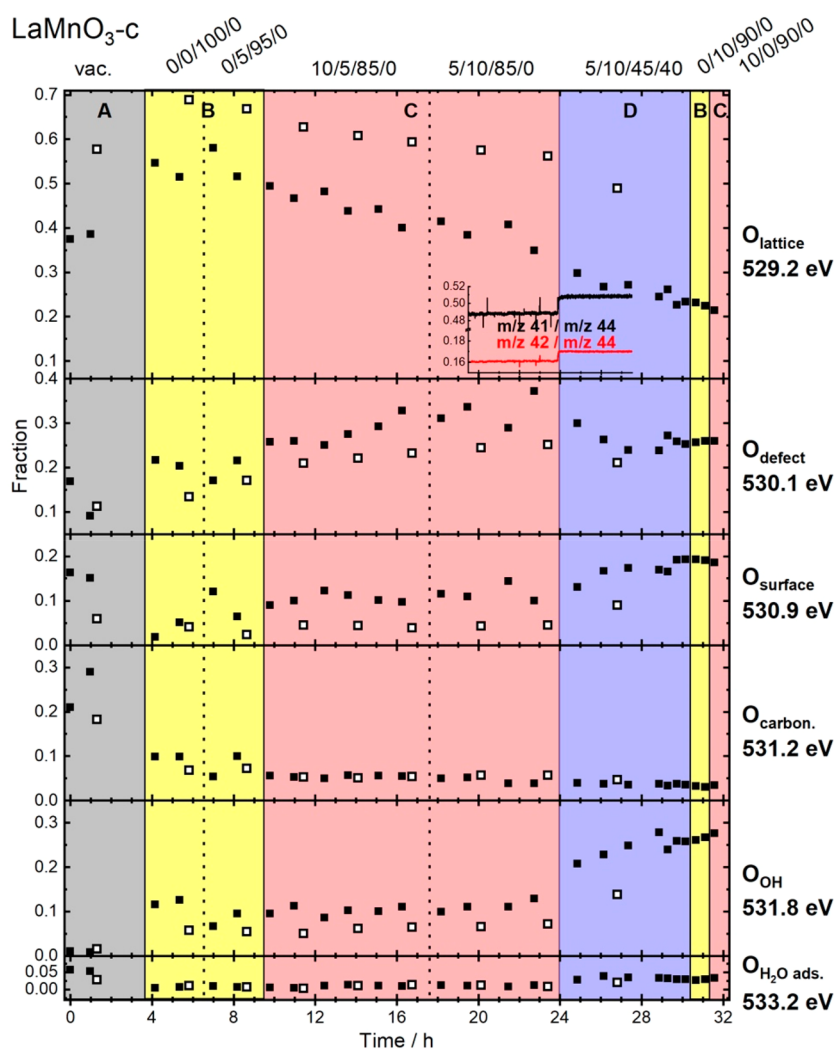


**Figure 7.** Fraction of oxygen species obtained from O 1s core level fitting of the AP-XPS spectra of LaMnO<sub>3</sub>-c. Spectra were conducted under different conditions, which are indicated at the top (the feed composition is specified as propane/O<sub>2</sub>/He/H<sub>2</sub>O) and summarized in areas A (gray - vacuum (vac) at room temperature and then at 270 °C for B (yellow, oxidative or inert atmosphere), C (red, propane oxidation feed), and D (blue, wet propane oxidation feed). After A and before B LaMnO<sub>3</sub>-c was heated at 5 °C min<sup>-1</sup> from 40 to 270 °C in 20% O<sub>2</sub> balanced by He. White squares denote spectra measured using 1300 eV excitation energy instead of 700 eV (black squares). The inset gives the ratio of ion currents of mass to charge ratio  $m/z$  41/44 (black) and  $m/z$  42/44 (red). The signals at  $m/z$  41 and 42 mainly represent propene, and that at  $m/z$  44 represents CO<sub>2</sub>.

The peak at a binding energy of 531.8 eV also behaves to some extent inverse to the signal of O<sub>defect</sub> during the pretreatment in 20% O<sub>2</sub> in He (Figure S14): i.e., it increases in intensity at low temperatures and decreases again above 150 °C while H<sub>2</sub>O is simultaneously released (water signal  $m/z$  18; see Figure S14). Therefore, and on the basis of the reported spectra of relevant hydroxides,<sup>62,68,69</sup> the signal at 531.8 eV is attributed to oxygen atoms in hydroxyl groups (O<sub>OH</sub>). The contribution exhibits the most distinct increase in a wet feed, which further supports the assignment (Figure 7 and Figure S15). The concurrent increase in the concentration of O<sub>OH</sub> and O<sub>surface</sub> (Figure 7 and Figure S15) and in particular the decrease in the concentration of O<sub>defect</sub> imply that defects are involved in water dissociation, resulting in filling the vacancies and forming OH groups.<sup>70</sup>

Finally, the peak at 533.2 eV is attributed to adsorbed molecular water. The weak tail in the range observed at room temperature between 534 and 535 eV is assigned to very small amounts of adsorbed oxygen-containing surface species,

respectively.<sup>71</sup> Their contributions diminish to zero at elevated temperatures; only molecular adsorbed H<sub>2</sub>O is still indicated in traces (Figure 7 and Figures S14 and S15).<sup>59</sup> This is reasonable because water is formed during the reaction or is cofed extensively when a wet feed is applied (Figures 6 and 7 and Figure S15). The quantification of this species is challenging, as its intensity is affected by the background subtraction and the exact choice of the peak shape.

On the basis of the assignment of O 1s peaks discussed above, changes on the catalyst surface during the pretreatment and reaction can be described as follows. During heating to 270 °C, all of the adsorbates are removed and the major part of the surface carbonate is also removed (Figure S14). This process is the same for both LaMnO<sub>3</sub>-c and SmMnO<sub>3</sub>-c. Thus, the stability of adsorbates and carbonates on the surface is independent of the A element.

The feed-sensitive structural changes in the near-surface region elucidated by *in situ* XPS were also the same for both LaMnO<sub>3</sub>-c and SmMnO<sub>3</sub>-c (compare Figure 7 and Figure

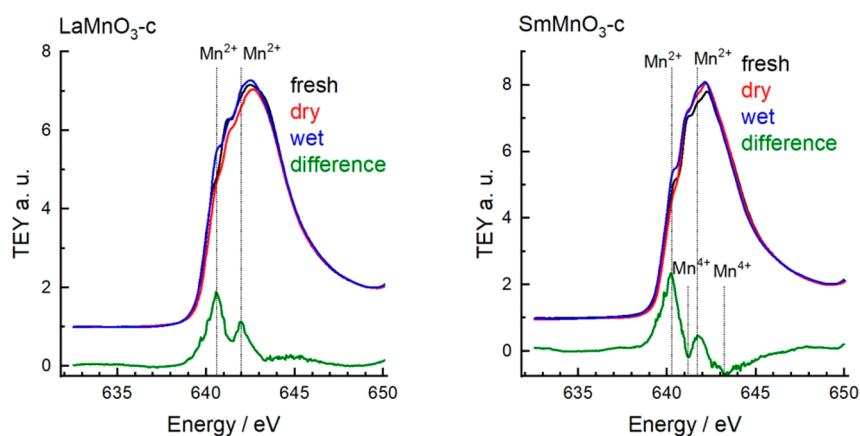


**Figure 8.** Normalized Mn  $L_{3,2}$  edge spectra of  $\text{LaMnO}_3\text{-c}$  (left) and  $\text{SmMnO}_3\text{-c}$  (right) conducted as fresh catalysts (black) and at  $270\text{ }^\circ\text{C}$  employing a dry propane oxidation feed (red; 5/10/85/0 propane/ $\text{O}_2$ /He/ $\text{H}_2\text{O}$ ) and after switching to wet feed (blue 5/10/45/40 propane/ $\text{O}_2$ /He/ $\text{H}_2\text{O}$ ). The difference spectrum obtained from a subtraction of wet feed (blue) from dry feed (red) spectra is given in green. Spectra are plotted with an offset.

S15). After a switch to a propane oxidation feed, the O 1s spectra change and the relative concentration of  $\text{O}_{\text{lattice}}$  is reduced, while the contributions of  $\text{O}_{\text{defect}}$  and  $\text{O}_{\text{surface}}$  increase and become more important.  $\text{O}_{\text{OH}}$  as well as  $\text{O}_{\text{surface}}$  represent about 10–20% of the detected oxygen species.

Interestingly, no formation of considerable amounts of carbonates is observed, although the formed  $\text{CO}_2$  can form carbonates under the moist conditions. Likewise, the surface concentration of  $\text{O}_{\text{OH}}$  changes only slightly, although water is formed as a couple product. The concentration of the corresponding surface species is apparently too small to be observed by XPS spectroscopy. The negligible poisoning of the catalyst by the reaction products  $\text{CO}_2$  and  $\text{H}_2\text{O}$  is also ascribed to the low conversion of propane reached in the *in situ* cell (<0.1%). In addition, the changes are small by switching from the oxygen-poor (10/5/85/0) to the oxygen-rich (5/10/85/0) dry propane oxidation feed.

However, when 40% of  $\text{H}_2\text{O}$  is added to the feed, a further decrease in  $\text{O}_{\text{lattice}}$  is observed (Figures 6B,D and 7 and Figure S15) indicating structural changes in the near-surface region. Remarkably, not only  $\text{O}_{\text{OH}}$  but also  $\text{O}_{\text{surface}}$  is increasing (Figure 7 and Figure S15). In the experiment with  $\text{SmMnO}_3\text{-c}$  (Figure S15), which was performed in shorter periods of time, the contribution of  $\text{O}_{\text{defect}}$  also increases in comparison to dry feed immediately after switching to wet feed but then decreases again in accordance with the observations made for  $\text{LaMnO}_3\text{-c}$  (Figure 7). The surface changes in wet feed are accompanied by an increase in selectivity to propene. The ratios of measured ion currents of  $m/z$  41 and 42, which come mainly from propene, and  $m/z$  44, which comes from  $\text{CO}_2$ , increase in a wet feed (Figure 7 and Figure S15, insets). These results reflect well the results obtained in catalytic testing in laboratory reactors (Figure 4). Again, as is observed in dry feed, the formation of surface carbonates is missing. The results suggest that in the presence of  $\text{H}_2\text{O}$  in the feed the coverage of the perovskite surface is changed. Both the increased concentration of OH species and the higher abundance of adsorbed activated oxygen apparently account for a more selective situation. The bulk of the perovskites seems to be rather unaffected by the feed, because feed-related changes are less pronounced using a higher excitation energy: i.e. 1300 eV (white squares in Figure 7 and Figure S15) instead of 700 eV (black squares in Figure 7 and Figure S15). If we remember

the different elemental distributions in the near-surface region of the perovskites under investigation, a higher selectivity to propene is achieved when Mn is enriched in the near surface (Figure 5). Hence, there are good reasons to assume a pronounced interaction of the  $\text{H}_2\text{O}$  in the feed with surface Mn–O bonds.<sup>68</sup> In summary, the concentration of the metals on the surface does not significantly vary under different gas-phase compositions at  $270\text{ }^\circ\text{C}$  (Figure 5), but defect concentration and coverage with oxygen species are affected (Figure 7 and Figure S15), which may have an effect on the formal oxidation state of Mn.

The electronic structure of the perovskite and the oxidation state of the B cation have been predicted to affect the reactivity of perovskites in terms of dissociative oxygen adsorption and oxygen vacancy formation energies.<sup>72</sup> The two reaction energies are of importance in oxidation catalysis regarding the activation of molecular oxygen and catalyst regeneration.<sup>73–75</sup> The mixed Mn valence is reflected in the Mn  $L_{3,2}$  edge spectra of the three catalysts (Figures S18 and S19). X-ray absorption at the  $L_{3,2}$  edge probes 3d orbital population and splitting; hence, both oxidation state and transition-metal site symmetry have an effect, which might complicate the analysis if distortion of the octahedra in the perovskites matters.<sup>76–78</sup> All spectra appear to represent a mixture of  $\text{Mn}^{3+}/\text{Mn}^{4+}$  in an octahedral environment.<sup>77</sup> The presence of  $\text{Mn}^{2+}$  cannot be excluded. The average oxidation state estimated from the NEXAFS fitting is given in Table 2. A comparison of the Mn  $L_{3,2}$  edge spectra of  $\text{LaMnO}_3\text{-c}$  and  $\text{SmMnO}_3\text{-c}$  measured under different conditions is depicted in Figure 8. Deviations in the spectra are visible especially in a switch from a dry (red) to a wet (blue) propane oxidation feed. The difference spectrum (green) that is obtained when the spectrum in wet feed is subtracted from the spectrum in dry feed resembles a Mn  $L_{3,2}$  edge spectrum of a  $\text{Mn}^{2+}$ -containing metal oxide. This observation agrees with a previous report in which the partial reduction of  $\text{Mn}^{3+}$  to  $\text{Mn}^{2+}$  as an effect of high  $\text{H}_2\text{O}$  vapor pressure in the gas phase has been shown for  $\text{LaMnO}_3$ .<sup>57</sup> The same applies to  $\text{SmMnO}_3\text{-c}$ . For  $\text{SmMnO}_3\text{-c}$ , a more pronounced second minimum is observed in the difference spectrum, which indicates the additional reduction of a minority  $\text{Mn}^{4+}$  fraction present in this material. The appearance of a  $\text{Mn}^{3+(4+)}/\text{Mn}^{2+}$  redox couple indicates similarities to nanostructured  $\text{MnWO}_4$  catalysts, in which

Mn<sup>3+</sup>/Mn<sup>2+</sup> was identified as the corresponding redox pair responsible for oxidation catalysis.<sup>28</sup> Moreover, the Mn<sup>3+</sup>/Mn<sup>2+</sup> redox couple has been regarded as important in the electrocatalytic oxygen reduction reaction on LaMnO<sub>3</sub> particles,<sup>42</sup> signifying parallels in oxygen activation in these two different processes over perovskite catalysts.

The partial reduction of Mn<sup>3+/4+</sup> to Mn<sup>2+</sup> species under the reaction conditions is also supported by the analysis of the Mn 3s splitting energy (Figures S20 and S21). According to Galakhov et al.,<sup>79</sup> the oxidation state of manganese in Mn-based perovskites can be roughly estimated, but with large uncertainties. Nevertheless, on the basis of an analysis of the Mn 3s splitting for LaMnO<sub>3-c</sub> (Figure S20) and SmMnO<sub>3-c</sub> (Figure S21), the reduction of the average oxidation state of Mn by switching from dry to wet feed is confirmed. Interestingly, the SmMnO<sub>3-c</sub> catalyst was oxidized during heating in 20% O<sub>2</sub> from formally +2.7 to +3.1 before applying feed (Figure S21). The average oxidation state of freshly prepared SmMnO<sub>3-c</sub> of +2.7 matches with the oxidation state +2.7 calculated on the basis of chemical analysis (Table 2). Moreover, the average oxidation state of Mn acquired from Mn 3s peak splitting analysis agrees well with the trends observed in the analysis of the Mn L<sub>3,2</sub> edges that indicates the presence of partially reduced Mn at 270 °C under wet propane oxidation conditions. The consistent results based on different analysis tools convincingly confirm the reliability of the observed trends and reveal that the surface oxidation state of Mn is sensitive toward different atmospheres in the employed low temperature range between room temperature and 270 °C.

The minor surface rearrangements observed in the present experiments might be a consequence of the limited concentration of oxygen vacancies near the surface in the applied mild reaction environment. Perovskites are frequently unstable under more severe conditions, such as in solid oxide fuel cells, because the high concentration of oxygen vacancies in the surface region leads to detrimental segregation of the A cation and even to phase separation due to electrostatic effects.<sup>80</sup> In the present investigation the surface composition is mainly controlled by the synthesis technique and pretreatment conditions. The high excess of La in case of the hydrothermally synthesized LaMnO<sub>3-h</sub>, which appears to be detrimental with respect to the selectivity in propane oxidation, is already evident at room temperature before the reaction. Consequently, the phase compositions of the spent catalysts remain unaffected and the reaction conditions in terms of temperature and feed composition have no significant effect on the elemental distribution on the surface (Figure 5). This is different from vanadium oxide based oxidation catalysts with open, nondense crystal structures, such as the so-called M1 structure, which show considerable surface dynamics with respect to element distribution and oxidation state of the redox-active element vanadium under the reaction conditions of propane oxidation depending on the feed composition.<sup>81,82</sup>

## ■ GENERAL DISCUSSION AND CONCLUSION

The Mn-based catalysts AMnO<sub>3</sub> (A = La, Sm) studied in the present work exhibit the formation of propene as the only selective oxidation product in the oxidation of propane. The exclusive product of deep oxidation and C–C bond splitting is CO<sub>2</sub>. Propene formation is favored by an excess of Mn on the surface of the catalyst. A high partial pressure of oxygen in the feed increases the activity and reduces the selectivity to propene. The negative effect of the oxygen partial pressure is

overcompensated for by addition of steam to the feed. The results further corroborate the concept of surface modification as an important tool to control the selectivity in oxidation catalysis over metal oxides.<sup>27,81,82</sup>

Steam in the feed causes a significant increase in selectivity to propene to values that become attractive for selective oxidation, in particular in case of the catalyst SmMnO<sub>3-c</sub>, which exhibits an excess of Mn on the surface. The elemental composition on the surface of the perovskite is primarily determined by the synthesis, because the surface concentration of Mn does not increase further due to wet conditions or reaction time. Under the applied reaction conditions neither structural changes nor segregation of phases occur.

AP-XPS reveals that the number of adsorbed water molecules is small at the reaction temperature, but the coverage with hydroxide species grows under consumption of defect sites when water vapor is added. Interestingly, another surface oxygen species, which is tentatively assigned to adsorbed activated oxygen, increases as well in wet feed, suggesting that both a high concentration of surface hydroxyl groups and the presence of electrophilic oxygen species on the surface have a positive effect on propene selectivity. The increase in the concentration of electrophilic surface species is in accordance with the simultaneous decrease in concentration of defect sites. It is necessary to investigate the nature of these species further by an application of complementary operando techniques.

Furthermore, the presence of steam in the feed gives rise to a lower overall oxidation state of the Mn<sup>n+</sup> surface ions ( $n \leq 3$ ) that appear as mixtures of Mn<sup>4+</sup> and Mn<sup>3+</sup> on the surface of the fresh catalysts. The sensitivity of the manganese oxidation state to the feed composition indicates that manganese is the redox-active element in propane oxidation, as in the oxygen reduction reaction over LaMnO<sub>3</sub>.<sup>42</sup>

Explicit clarification of the effect of water on the reaction mechanism requires detailed mechanistic investigations. The current *in situ* experiments provide awareness about coverage changes on the surface in terms of hydroxyl groups and adsorbed oxygen species and a reduction in the valence state of the B cation. These changes may have implications on either site isolation or the regeneration mechanism of the catalyst.

The performance of perovskites in alkane oxidation indicates that they are hyperactive with respect to selective oxidation of the desired products, of which oxygenates are intermediates on the way from the alkane to CO<sub>2</sub>. The present work showed that surface modification by interfering with abundance, cation ordering, and local electronic structure of the B cation is a powerful strategy to moderate the hyperactivity. Two avenues of modifications were found: namely, by synthetic measures favoring Mn overabundance and by process conditions favoring modification of anion vacancies and surface coverage. Redox changes of the Mn near-surface species were reflected in the abundance of surface oxygen likely being essential for activating propane.

It is a fortuitous property of the present perovskites that the formation of a termination layer and its adaptation to changes in chemical potential can occur without having to change the cubic base of the structure. No structure-induced segregation and no irreversible breakdown of the translational order are necessary. This ensures a facile response of the system to changes in the reactant phase and little propensity to the formation of inactive (A cation) or detrimental deactivation products (binary Mn oxides). Such behavior is similar to that

of the highly stable and well-performing M1 phase that undergoes reversible dynamic surface modifications.<sup>81</sup> This encourages further efforts in improving the performance of these systems toward practical application.

Further studies need to identify the function of the B cation modification. In addition to a direct interference with the activation of reactants, the modification may also affect the kinetics of active site formation and regeneration (the chemical dynamics) of the system. The present work highlights in broader terms that the identification of a suitable catalyst must not stop at the preparation of a single phase as judged from its translational structure. Rather, the details of the real structure in the near-surface region has to be optimized for a desired function. A single preparation of a phase in high-throughput search strategies may easily end up with an unsuitable surface termination and thus discredit the potential of a phase as a catalyst. The present work calls for a modification of such strategies examining families of compounds of the same translational structure synthesized under different conditions so as to modify the near-surface region.

## ■ ASSOCIATED CONTENT

### ■ Supporting Information

The Supporting Information is available free of charge at <https://pubs.acs.org/doi/10.1021/acscatal.0c01289>.

Catalytic test protocol and data analysis, AP-XPS measurement conditions and O 1s fitting model, Raman measurement conditions, laboratory XPS of fresh and spent catalysts, XRD patterns of fresh catalysts, HAADF-STEM of fresh catalysts, EELS spectra and STEM-HAADF image of bulk and surface, propane oxidation in different feeds, temperature-programmed reduction, propane oxidation at high temperatures, W/F variation at 300 °C in propane oxidation, XRD patterns of spent catalysts, HAADF-STEM of spent catalysts, O 1s spectra during temperature-programmed and *in situ* experiments, Mn L<sub>3,2</sub> edge spectra of fresh catalysts under vacuum at room temperature, Mn L<sub>3,2</sub> edge reference spectra, and calculated Mn oxidation states determined by AP-XPS under different operation conditions (PDF)

## ■ AUTHOR INFORMATION

### Corresponding Author

**Annette Trunschke** – Fritz-Haber-Institut der Max-Planck-Gesellschaft, 14195 Berlin, Germany; [orcid.org/0000-0003-2869-0181](https://orcid.org/0000-0003-2869-0181); Email: [trunschke@fhi-berlin.mpg.de](mailto:trunschke@fhi-berlin.mpg.de)

### Authors

**Gregor Koch** – Fritz-Haber-Institut der Max-Planck-Gesellschaft, 14195 Berlin, Germany

**Michael Hävecker** – Fritz-Haber-Institut der Max-Planck-Gesellschaft, 14195 Berlin, Germany; Max-Planck-Institut für Chemische Energiekonversion, 45470 Mülheim, Germany

**Detre Teschner** – Fritz-Haber-Institut der Max-Planck-Gesellschaft, 14195 Berlin, Germany; Max-Planck-Institut für Chemische Energiekonversion, 45470 Mülheim, Germany

**Spencer J. Carey** – Fritz-Haber-Institut der Max-Planck-Gesellschaft, 14195 Berlin, Germany

**Yuanqing Wang** – Fritz-Haber-Institut der Max-Planck-Gesellschaft, 14195 Berlin, Germany; BasCat - UniCat BASF

JointLab, Technische Universität Berlin, 10623 Berlin, Germany; [orcid.org/0000-0002-1332-7956](https://orcid.org/0000-0002-1332-7956)

**Pierre Kube** – Fritz-Haber-Institut der Max-Planck-Gesellschaft, 14195 Berlin, Germany

**Walid Hetaba** – Fritz-Haber-Institut der Max-Planck-Gesellschaft, 14195 Berlin, Germany; Max-Planck-Institut für Chemische Energiekonversion, 45470 Mülheim, Germany

**Thomas Lunkenbein** – Fritz-Haber-Institut der Max-Planck-Gesellschaft, 14195 Berlin, Germany; [orcid.org/0000-0002-8957-4216](https://orcid.org/0000-0002-8957-4216)

**Gudrun Auffermann** – Max-Planck-Institut für Chemische Physik fester Stoffe, 01187 Dresden, Germany

**Olaf Timpe** – Fritz-Haber-Institut der Max-Planck-Gesellschaft, 14195 Berlin, Germany

**Frank Rosowski** – BASF SE, Process Research and Chemical Engineering, Heterogeneous Catalysis, 67056 Ludwigshafen, Germany

**Robert Schlögl** – Fritz-Haber-Institut der Max-Planck-Gesellschaft, 14195 Berlin, Germany; Max-Planck-Institut für Chemische Energiekonversion, 45470 Mülheim, Germany

Complete contact information is available at: <https://pubs.acs.org/10.1021/acscatal.0c01289>

### Notes

The authors declare no competing financial interest.

## ■ ACKNOWLEDGMENTS

This work was conducted in the framework of the BasCat collaboration among BASF SE, Technical University Berlin, Fritz-Haber-Institut der Max-Planck-Gesellschaft, and the cluster of excellence “Unified Concepts in Catalysis” (UniCat <http://www.unicat.tu-berlin.de>). We thank Stephen Lohr for his support during synthesis, Dr. Frank Girgsdies and Jasmin Allan for performing XRD measurements, Maike Hashagen for N<sub>2</sub> adsorption measurements, and Prof. Evgeny V. Antipov and Dr. Sergey Ya. Istomin, Lomonosov State University, Moscow, for stimulating discussions. The Helmholtz-Zentrum Berlin is acknowledged for providing beamtime (proposal numbers 172-05966 and 191-08014) and for the continuous support of the ambient-pressure XPS activities of the MPG at BESSY.

## ■ REFERENCES

- (1) Hirose, K.; Sinmyo, R.; Hernalund, J. Perovskite in Earth's deep interior. *Science* **2017**, *358*, 734–738.
- (2) Voorhoeve, R. J. H.; Johnson, D. W.; Remeika, J. P.; Gallagher, P. K. Perovskite Oxides: Materials Science in Catalysis. *Science* **1977**, *195*, 827–833.
- (3) Goodenough, J. B. Electronic and ionic transport properties and other physical aspects of perovskites. *Rep. Prog. Phys.* **2004**, *67*, 1915–1993.
- (4) Suntivich, J.; May, K. J.; Gasteiger, H. A.; Goodenough, J. B.; Shao-Horn, Y. A Perovskite Oxide Optimized for Oxygen Evolution Catalysis from Molecular Orbital Principles. *Science* **2011**, *334*, 1383–1385.
- (5) Seh, Z. W.; Kibsgaard, J.; Dickens, C. F.; Chorkendorff, I.; Nørskov, J. K.; Jaramillo, T. F. Combining theory and experiment in electrocatalysis: Insights into materials design. *Science* **2017**, *355*, No. eaad4998.
- (6) Tanaka, H.; Misono, M. Advances in designing perovskite catalysts. *Curr. Opin. Solid State Mater. Sci.* **2001**, *5*, 381–387.
- (7) Klissurski, D.; Rives, V. High-temperature superconductors in catalysis. *Appl. Catal., A* **1994**, *109*, 1–44.
- (8) Grimaud, A.; May, K. J.; Carlton, C. E.; Lee, Y.-L.; Risch, M.; Hong, W. T.; Zhou, J.; Shao-Horn, Y. Double perovskites as a family

of highly active catalysts for oxygen evolution in alkaline solution. *Nat. Commun.* **2013**, *4*, 2439.

(9) Grabowska, E. Selected perovskite oxides: Characterization, preparation and photocatalytic properties — A review. *Appl. Catal., B* **2016**, *186*, 97–126.

(10) Royer, S.; Duprez, D.; Can, F.; Courtois, X.; Batiot-Dupeyrat, C.; Laassiri, S.; Alamdari, H. Perovskites as substitutes of noble metals for heterogeneous catalysis: dream or reality. *Chem. Rev.* **2014**, *114*, 10292–10368.

(11) Zhu, J.; Li, H.; Zhong, L.; Xiao, P.; Xu, X.; Yang, X.; Zhao, Z.; Li, J. Perovskite Oxides: Preparation, Characterizations, and Applications in Heterogeneous Catalysis. *ACS Catal.* **2014**, *4*, 2917–2940.

(12) Marchetti, L.; Forni, L. Catalytic combustion of methane over perovskites. *Appl. Catal., B* **1998**, *15*, 179–187.

(13) Merino, N. A.; Barbero, B. P.; Grange, P.; Cadús, L. E.  $\text{La}_{1-x}\text{Ca}_x\text{CoO}_3$  perovskite-type oxides: preparation, characterisation, stability, and catalytic potentiality for the total oxidation of propane. *J. Catal.* **2005**, *231*, 232–244.

(14) Rousseau, S.; Lorient, S.; Delichere, P.; Boreave, A.; Deloume, J. P.; Vernoux, P.  $\text{La}_{1-x}\text{Sr}_x\text{Co}_{1-y}\text{Fe}_y\text{O}_3$  perovskites prepared by sol–gel method: Characterization and relationships with catalytic properties for total oxidation of toluene. *Appl. Catal., B* **2009**, *88*, 438–447.

(15) ten Elshof, J. E.; Bouwmeester, H. J. M.; Verweij, H. Oxidative coupling of methane in a mixed-conducting perovskite membrane reactor. *Appl. Catal., A* **1995**, *130*, 195–212.

(16) Wei, Y.; Yang, W.; Caro, J.; Wang, H. Dense ceramic oxygen permeable membranes and catalytic membrane reactors. *Chem. Eng. J.* **2013**, *220*, 185–203.

(17) Yang, W.; Wang, H.; Zhu, X.; Lin, L. Development and Application of Oxygen Permeable Membrane in Selective Oxidation of Light Alkanes. *Top. Catal.* **2005**, *35*, 155–167.

(18) Basini, L.; Cimino, S.; Guarinoni, A.; Russo, G.; Arca, V. Olefins via catalytic partial oxidation of light alkanes over Pt/LaMnO<sub>3</sub> monoliths. *Chem. Eng. J.* **2012**, *207*–208, 473–480.

(19) Watanabe, R.; Hondo, Y.; Mukawa, K.; Fukuhara, C.; Kikuchi, E.; Sekine, Y. Stable and selective perovskite catalyst for dehydrogenation of propane working with redox mechanism. *J. Mol. Catal. A: Chem.* **2013**, *377*, 74–84.

(20) Watanabe, R.; Tsujioka, M.; Fukuhara, C. Performance of Non-stoichiometric Perovskite Catalyst ( $\text{A}_x\text{CrO}_{3-\delta}$ , A: La, Pr, Nd) for Dehydrogenation of Propane Under Steam Condition. *Catal. Lett.* **2016**, *146*, 2458–2467.

(21) Gao, Y.; Haeri, F.; He, F.; Li, F. Alkali Metal-Promoted  $\text{La}_x\text{Sr}_{2-x}\text{FeO}_{4-\delta}$  Redox Catalysts for Chemical Looping Oxidative Dehydrogenation of Ethane. *ACS Catal.* **2018**, *8*, 1757–1766.

(22) Crapanzano, S.; Babich, I. V.; Loefferts, L. The influence of over-stoichiometry in  $\text{La}_2\text{Ni}_{0.9}\text{V}_{0.1}\text{O}_{4.15+\delta}$  on selective oxidative dehydrogenation of propane. *Catal. Today* **2013**, *203*, 17–23.

(23) Grant, J. T.; Venegas, J. M.; McDermott, W. P.; Hermans, I. Aerobic Oxidations of Light Alkanes over Solid Metal Oxide Catalysts. *Chem. Rev.* **2018**, *118*, 2769–2815.

(24) Cheng, M.-J.; Goddard, W. A. The Critical Role of Phosphate in Vanadium Phosphate Oxide for the Catalytic Activation and Functionalization of n-Butane to Maleic Anhydride. *J. Am. Chem. Soc.* **2013**, *135*, 4600–4603.

(25) Zhu, Y.; Sushko, P. V.; Melzer, D.; Jensen, E.; Kovarik, L.; Ophus, C.; Sanchez-Sanchez, M.; Lercher, J. A.; Browning, N. D. Formation of Oxygen Radical Sites on MoVNbTeOx by Cooperative Electron Redistribution. *J. Am. Chem. Soc.* **2017**, *139*, 12342–12345.

(26) Cheng, M.-J.; Goddard, W. A. In Silico Design of Highly Selective Mo-V-Te-Nb-O Mixed Metal Oxide Catalysts for Ammonia Oxidation and Oxidative Dehydrogenation of Propane and Ethane. *J. Am. Chem. Soc.* **2015**, *137*, 13224–13227.

(27) Eichelbaum, M.; Hävecker, M.; Heine, C.; Wernbacher, A. M.; Rosowski, F.; Trunschke, A.; Schlögl, R. The Electronic Factor in Alkane Oxidation Catalysis. *Angew. Chem., Int. Ed.* **2015**, *54*, 2922–2926.

(28) Li, X.; Lunkenbein, T.; Pfeifer, V.; Jastak, M.; Nielsen, P. K.; Girgsdies, F.; Knop-Gericke, A.; Rosowski, F.; Schlögl, R.; Trunschke, A. Selective Alkane Oxidation by Manganese Oxide: Site Isolation of MnO<sub>x</sub> Chains at the Surface of MnWO<sub>4</sub> Nanorods. *Angew. Chem., Int. Ed.* **2016**, *55*, 4092–4096.

(29) Pechini, P. M. Method of preparing lead and alkaline earth titanates and niobates and coating method using the same to form a capacitor. US Patent 3330697, 1967.

(30) Bernard, C.; Dauzet, G.; Mathieu, F.; Durand, B.; Puech-Costes, E. Optimization of the hydrothermal synthesis of  $\text{La}_{0.7}\text{Sr}_{0.3}\text{MnO}_{3+\delta}$  using an original optimal experimental design. *Mater. Lett.* **2005**, *59*, 2615–2620.

(31) Bernard, C.; Laberty, C.; Ansart, F.; Durand, B. Hydrothermal synthesis of  $\text{La}_{1-x}\text{Sr}_x\text{MnO}_{3+\delta}$  manganites. *Ann. Chim.* **2003**, *28*, 85–96.

(32) Knop-Gericke, A.; Kleimenov, E.; Hävecker, M.; Blume, R.; Teschner, D.; Zafeiratos, S.; Schlögl, R.; Bukhtiyarov, V. I.; Kaichev, V. V.; Prosvirni, I. P.; Nizovskii, A. I.; Bluhm, H.; Barinov, A.; Dudin, P.; Kiskinova, M. Chapter 4 X-Ray Photoelectron Spectroscopy for Investigation of Heterogeneous Catalytic Processes. *Adv. Catal.* **2009**, *52*, 213–272.

(33) Salmeron, M.; Schlögl, R. Ambient pressure photoelectron spectroscopy: A new tool for surface science and nanotechnology. *Surf. Sci. Rep.* **2008**, *63*, 169–199.

(34) Miyoshi, S.; Hong, J.-O.; Yashiro, K.; Kaimai, A.; Nigara, Y.; Kawamura, K.; Kawada, T.; Mizusaki, J. Lattice expansion upon reduction of perovskite-type  $\text{LaMnO}_3$  with oxygen-deficit non-stoichiometry. *Solid State Ionics* **2003**, *161*, 209–217.

(35) Ullmann, H.; Trofimenko, N. Estimation of effective ionic radii in highly defective perovskite-type oxides from experimental data. *J. Alloys Compd.* **2001**, *316*, 153–158.

(36) Samira, S.; Gu, X.-K.; Nikolla, E. Design Strategies for Efficient Nonstoichiometric Mixed Metal Oxide Electrocatalysts: Correlating Measurable Oxide Properties to Electrocatalytic Performance. *ACS Catal.* **2019**, *9*, 10575–10586.

(37) Töpfer, J.; Goodenough, J. B.  $\text{LaMnO}_{3+d}$  Revised. *J. Solid State Chem.* **1997**, *130*, 117–128.

(38) van Roosmalen, J. A. M.; van Vlaanderen, P.; Cordfunke, E. H. P. Phases of the Perovskite-Type  $\text{LaMnO}_{3+\delta}$  Solid Solution and the  $\text{La}_2\text{O}_3\text{-Mn}_2\text{O}_3$  Phase Diagram. *J. Solid State Chem.* **1995**, *114*, 516–523.

(39) Golikov, Y. V.; Balakirev, V. F.; Fedorova, O. M. Homogeneity Range of Samarium Manganite in Air. *Inorg. Mater.* **2005**, *41*, 1010–1012.

(40) Wolcyz, M.; Horyń, R.; Bourée, F.; Bukowska, E. Structural defects in  $\text{LaMnO}_3$  phase studied by neutron diffraction. *J. Alloys Compd.* **2003**, *353*, 170–174.

(41) De Souza, R. A.; Saiful Islam, M.; Ivers-Tiffée, E. Formation and migration of cation defects in the perovskite oxide  $\text{LaMnO}_3$ . *J. Mater. Chem.* **1999**, *9*, 1621–1627.

(42) Ignatans, R.; Mallia, G.; Ahmad, E. A.; Spillane, L.; Stoerzinger, K. A.; Shao-Horn, Y.; Harrison, N. M.; Tileli, V. The Effect of Surface Reconstruction on the Oxygen Reduction Reaction Properties of  $\text{LaMnO}_3$ . *J. Phys. Chem. C* **2019**, *123*, 11621–11627.

(43) Iliev, M. N.; Abrashev, M. V.; Lee, H.-G.; Popov, V. N.; Sun, Y. Y.; Thomsen, C.; Meng, R. L.; Chu, C. W. Raman spectroscopy of orthorhombic perovskitelike  $\text{YMnO}_3$  and  $\text{LaMnO}_3$ . *Phys. Rev. B: Condens. Matter Mater. Phys.* **1998**, *57*, 2872–2877.

(44) Iliev, M. N.; Abrashev, M. V. Raman phonons and Raman Jahn-Teller bands in perovskite-like manganites. *J. Raman Spectrosc.* **2001**, *32*, 805–811.

(45) Iliev, M. N.; Abrashev, M. V.; Popov, V. N.; Hadjiev, V. G. Role of Jahn-Teller disorder in Raman scattering of mixed-valence manganites. *Phys. Rev. B: Condens. Matter Mater. Phys.* **2003**, *67*, 212301.

(46) Krüger, R.; Schulz, B.; Naler, S.; Rauer, R.; Budelmann, D.; Bäckström, J.; Kim, K. H.; Cheong, S. W.; Perebeinos, V.; Rübhausen, M. Orbital ordering in  $\text{LaMnO}_3$  Investigated by Resonance Raman Spectroscopy. *Phys. Rev. Lett.* **2004**, *92*, 097203.

- (47) Li, X.; Teschner, D.; Streibel, V.; Lunkenbein, T.; Masliuk, L.; Fu, T.; Wang, Y.; Jones, T.; Seitz, F.; Girgsdies, F.; Rosowski, F.; Schlögl, R.; Trunschke, A. How to control selectivity in alkane oxidation? *Chem. Sci.* **2019**, *10*, 2429–2443.
- (48) Buciuman, F.; Patcas, F.; Craciun, R.; Zahn, D. R. T. Vibrational spectroscopy of bulk and supported manganese oxides. *Phys. Chem. Chem. Phys.* **1999**, *1*, 185–190.
- (49) Miniajluk, N.; Trawczyński, J.; Zawadzki, M. Properties and catalytic performance for propane combustion of LaMnO<sub>3</sub> prepared under microwave-assisted glycothermal conditions: Effect of solvent diols. *Appl. Catal., A* **2017**, *531*, 119–128.
- (50) Taguchi, H.; Sugita, A.; Nagao, M.; Tabata, K. Surface Characterization of LaMnO<sub>3+δ</sub> Powder Annealed in Air. *J. Solid State Chem.* **1995**, *119*, 164–168.
- (51) Esmaeilnejad-Ahranjani, P.; Khodadadi, A.; Ziaei-Azad, H.; Mortazavi, Y. Effects of excess manganese in lanthanum Manganite perovskite on lowering oxidation light-off temperature for automotive exhaust gas pollutants. *Chem. Eng. J.* **2011**, *169*, 282–289.
- (52) Kube, P.; Frank, B.; Wrabetz, S.; Kröhnert, J.; Hävecker, M.; Velasco-Vélez, J.; Noack, J.; Schlögl, R.; Trunschke, A. Functional Analysis of Catalysts for Lower Alkane Oxidation. *ChemCatChem* **2017**, *9*, 573–585.
- (53) Kube, P.; Frank, B.; Schlögl, R.; Trunschke, A. Isotope Studies in Oxidation of Propane over Vanadium Oxide. *ChemCatChem* **2017**, *9*, 3446–3455.
- (54) Sup Song, K.; Klvana, D.; Kirchnerova, J. Kinetics of propane combustion over La<sub>0.66</sub>Sr<sub>0.34</sub>Ni<sub>0.3</sub>Co<sub>0.7</sub>O<sub>3</sub> perovskite. *Appl. Catal., A* **2001**, *213*, 113–121.
- (55) Billman, C. R.; Wang, Y.; Cheng, H. P. Water adsorption on the LaMnO<sub>3</sub> surface. *J. Chem. Phys.* **2016**, *144*, 064701.
- (56) Oyama, S. T.; Middlebrook, A. M.; Somorjai, G. A. Kinetics of ethane oxidation on vanadium oxide. *J. Phys. Chem.* **1990**, *94*, 5029–5033.
- (57) Mierwaldt, D.; Mildner, S.; Arrigo, R.; Knop-Gericke, A.; Franke, E.; Blumenstein, A.; Hoffmann, J.; Jooss, C. In Situ XANES/XPS Investigation of Doped Manganese Perovskite Catalysts. *Catalysts* **2014**, *4*, 129–145.
- (58) Stoerzinger, K. A.; Hong, W. T.; Azimi, G.; Giordano, L.; Lee, Y.-L.; Crumlin, E. J.; Biegalski, M. D.; Bluhm, H.; Varanasi, K. K.; Shao-Horn, Y. Reactivity of Perovskites with Water: Role of Hydroxylation in Wetting and Implications for Oxygen Electrocatalysis. *J. Phys. Chem. C* **2015**, *119*, 18504–18512.
- (59) Stoerzinger, K. A.; Hong, W. T.; Crumlin, E. J.; Bluhm, H.; Biegalski, M. D.; Shao-Horn, Y. Water Reactivity on the LaCoO<sub>3</sub> (001) Surface: An Ambient Pressure X-ray Photoelectron Spectroscopy Study. *J. Phys. Chem. C* **2014**, *118*, 19733–19741.
- (60) Walton, J.; Wincott, P.; Fairley, N.; Carrick, A. *Peak Fitting with CasaXPS*; Accolyte Science: Knutsford, U.K., 2010.
- (61) Najjar, H.; Lamonier, J.-F.; Mentré, O.; Giraudon, J.-M.; Batis, H. Optimization of the combustion synthesis towards efficient LaMnO<sub>3+δ</sub> catalysts in methane oxidation. *Appl. Catal., B* **2011**, *106*, 149–159.
- (62) Sunding, M. F.; Hadidi, K.; Diplas, S.; Løvvik, O. M.; Norby, T. E.; Gunnæs, A. E. XPS characterisation of in situ treated lanthanum oxide and hydroxide using tailored charge referencing and peak fitting procedures. *J. Electron Spectrosc. Relat. Phenom.* **2011**, *184*, 399–409.
- (63) Evarestov, R. A.; Kotomin, E. A.; Fuks, D.; Felsteiner, J.; Maier, J. Ab initio calculations of the LaMnO<sub>3</sub> surface properties. *Appl. Surf. Sci.* **2004**, *238*, 457–463.
- (64) Evarestov, R. A.; Kotomin, E. A.; Heifets, E.; Maier, J.; Borstel, G. Ab initio Hartree-Fock calculations of LaMnO<sub>3</sub> (110) surfaces. *Solid State Commun.* **2003**, *127*, 367–371.
- (65) Yamazoe, N.; Teraoka, Y.; Seiyama, T. TPD and XPS study on thermal behaviour of absorbed oxygen in La<sub>1-x</sub>Sr<sub>x</sub>CoO<sub>3</sub>. *Chem. Lett.* **1981**, *10*, 1767–1770.
- (66) Merkle, R.; Maier, J. How Is Oxygen Incorporated into Oxides? A Comprehensive Kinetic Study of a Simple Solid-State Reaction with SrTiO<sub>3</sub> as a Model Material. *Angew. Chem., Int. Ed.* **2008**, *47*, 3874–3894.
- (67) Xia, X.; Oldman, R. J.; Catlow, C. R. A. Oxygen adsorption and dissociation on yttria stabilized zirconia surfaces. *J. Mater. Chem.* **2012**, *22*, 8594–8612.
- (68) Li, F.; Zhang, L.; Evans, D. G.; Duan, X. Structure and surface chemistry of manganese-doped copper-based mixed metal oxides derived from layered double hydroxides. *Colloids Surf., A* **2004**, *244*, 169–177.
- (69) Nesbitt, H. W.; Banerjee, D. Interpretation of XPS Mn(2p) spectra of Mn oxyhydroxides and constraints on the mechanism of MnO<sub>2</sub> precipitation. *Am. Mineral.* **1998**, *83*, 305–315.
- (70) Coulaud, E.; Dezanneau, G.; Geneste, G. Hydration, oxidation, and reduction of GdBaCo<sub>2</sub>O<sub>5.5</sub> from first-principles. *J. Mater. Chem. A* **2015**, *3*, 23917–23929.
- (71) Ponce, S. P.; M, A.; Fierro, J. L. G. , Surface properties and catalytic performance in methane combustion of Sr-substituted Lanthanum manganites. *Appl. Catal., B* **2000**, *24*, 193–205.
- (72) Akhade, S. A.; Kitchin, J. R. Effects of strain, d-band filling, and oxidation state on the surface electronic structure and reactivity of 3d perovskite surfaces. *J. Chem. Phys.* **2012**, *137*, 084703.
- (73) Gellings, P. J.; Bouwmeester, H. J. M. Solid state aspects of oxidation catalysis. *Catal. Today* **2000**, *58*, 1–53.
- (74) McFarland, E. W.; Metiu, H. Catalysis by Doped Oxides. *Chem. Rev.* **2013**, *113*, 4391–4427.
- (75) Dickens, C. F.; Montoya, J. H.; Kulkarni, A. R.; Bajdich, M.; Nørskov, J. K. An electronic structure descriptor for oxygen reactivity at metal and metal-oxide surfaces. *Surf. Sci.* **2019**, *681*, 122–129.
- (76) Cramer, S. P.; DeGroot, F. M. F.; Ma, Y.; Chen, C. T.; Sette, F.; Kipke, C. A.; Eichhorn, D. M.; Chan, M. K.; Armstrong, W. H. Ligand field strengths and oxidation states from manganese L-edge spectroscopy. *J. Am. Chem. Soc.* **1991**, *113*, 7937–7940.
- (77) Gilbert, B.; Frazer, B. H.; Belz, A.; Conrad, P. G.; Neelson, K. H.; Haskel, D.; Lang, J. C.; Srajer, G.; De Stasio, G. Multiple Scattering Calculations of Bonding and X-ray Absorption Spectroscopy of Manganese Oxides. *J. Phys. Chem. A* **2003**, *107*, 2839–2847.
- (78) Garvie, L. A. J.; Craven, A. J. High-resolution Parallel Electron Energy-loss Spectroscopy of Mn L<sub>2,3</sub>-Edges in Inorganic Manganese Compounds. *Phys. Chem. Miner.* **1994**, *21*, 191–206.
- (79) Galakhov, V. R.; Demeter, M.; Bartkowski, S.; Neumann, M.; Ovechikina, N. A.; Kurmaev, E. Z.; Lobachevskaya, N. I.; Mukovskii, Y. M.; Mitchell, J.; Ederer, D. L. Mn3s exchange splitting in mixed-valence manganites. *Phys. Rev. B: Condens. Matter Mater. Phys.* **2002**, *65*, 113102.
- (80) Tsvetkov, N.; Lu, Q.; Sun, L.; Crumlin, E. J.; Yildiz, B. Improved chemical and electrochemical stability of perovskite oxides with less reducible cations at the surface. *Nat. Mater.* **2016**, *15*, 1010–1016.
- (81) Hävecker, M.; Wrabetz, S.; Kröhnert, J.; Csepei, L.-I.; Naumann d'Alnoncourt, R.; Kolen'ko, Y. V.; Girgsdies, F.; Schlögl, R.; Trunschke, A. Surface chemistry of phase-pure M1MoVTenb oxide during operation in selective oxidation of propane to acrylic acid. *J. Catal.* **2012**, *285*, 48–60.
- (82) Trunschke, A.; Noack, J.; Trojanov, S.; Girgsdies, F.; Lunkenbein, T.; Pfeifer, V.; Hävecker, M.; Kube, P.; Sprung, C.; Rosowski, F.; Schlögl, R. The Impact of the Bulk Structure on Surface Dynamics of Complex Mo–V-based Oxide Catalysts. *ACS Catal.* **2017**, *7*, 3061–3071.